nature portfolio

Peer Review File

Machine learning-powered activatable NIR-II fluorescent nanosensor for in vivo monitoring of plant stress responses

Corresponding Author: Professor Yixian Wang

This file contains all reviewer reports in order by version, followed by all author rebuttals in order by version.

Attachments originally included by the reviewers as part of their assessment can be found at the end of this file.

Version 0:

Reviewer comments:

Reviewer #1

(Remarks to the Author)
Review comments attached.

Reviewer #2

(Remarks to the Author)
I co-reviewed this manuscript with one of the reviewers who provided the listed reports. This is part of the Nature Communications initiative to facilitate training in peer review and to provide appropriate recognition for Early Career Researchers who co-review manuscripts.

Reviewer #3

(Remarks to the Author)
The manuscript presents an innovative approach by integrating machine-learning-powered NIR-II fluorescent nanosensors for real-time, non-invasive monitoring of plant stress responses, specifically focusing on H_2O_2 signaling. The study showcases a strong experimental foundation and demonstrates the application of the technology across multiple plant species. However, some areas require further elaboration and clarification. Below is a detailed review:

The strengths of this work are evident. The integration of a fluorescence "turn-on" mechanism with machine learning to classify stress types is a major contribution to the field of agricultural diagnostics. The nanosensor's ability to bypass background autofluorescence and provide real-time, species-independent stress monitoring addresses key limitations in current plant sensing technologies. Furthermore, the study demonstrates impressive validation across various plant species, solidifying the robustness and universality of the approach. The use of machine learning, particularly XGBoost, for stress classification and its high accuracy of up to 96.67% for identifying specific stressors adds a layer of scalability and applicability to the technology.

Despite these strengths, the manuscript has some weaknesses and areas for improvement:

1.The introduction could better contextualize the limitations of existing technologies by offering a detailed comparison of their shortcomings.

2.The manuscript does not address the scalability of this approach for field applications, which is critical for its adoption in agriculture.

3.The potential long-term impacts of introducing nanosensors on plant health and soil ecosystems are not discussed.

4.The use of machine learning in the study is commendable but lacks depth in explaining how features were extracted and used for stress classification. Furthermore, it is unclear whether the model would generalize well to untrained plant species

or stress types. The authors could expand on the interpretability and adaptability of their machine learning mode.

5.While the study mentions diffusion limitations of nanosensors within plant tissues, it does not propose solutions or alternative delivery methods to overcome this challenge.

6.A comparative analysis with existing state-of-the-art sensors (not limited to other NIR sensors), particularly in terms of cost, sensitivity, and ease of deployment, is missing and would strengthen the study's relevance.

7.How does the nanosensor perform under open-field conditions with fluctuating environmental factors such as humidity, wind, and soil variability?

8.What is the estimated lifespan of the nanosensors when deployed on plants? Are the sensors reusable, or are they intended for single use?

9.Could this nanosensor technology be adapted to detect other plant signaling molecules, potentially broadening its applicability to other agricultural or environmental diagnostics?

Version 1:

Reviewer comments:

Reviewer #1

(Remarks to the Author)
I am satisfied with the authors' revisions and do not have further comments. I believe it can be considered for publication in Nature Communications now.

Reviewer #2

(Remarks to the Author)
I co-reviewed this manuscript with one of the reviewers who provided the listed reports. This is part of the Nature Communications initiative to facilitate training in peer review and to provide appropriate recognition for Early Career Researchers who co-review manuscripts.

Reviewer #3

(Remarks to the Author)
I appreciate the thorough and thoughtful responses to my previous comments. The authors have clearly made substantial revisions to the manuscript, including additional experimental data, expanded discussion on scalability and environmental impact, and a much more comprehensive treatment of the machine learning implementation. These improvements significantly strengthen the manuscript.
As a suggestion to further enhance clarity for readers interested in real-world applications, it might be helpful to include a schematic or dedicated paragraph outlining the envisioned field deployment workflow — from nanosensor administration to signal acquisition and ML-based classification. This would help bridge the gap between lab-based validation and practical agricultural use cases.
That aside, I have no further concerns, and I believe the paper is now suitable for publication.

Responses to Reviewers' Comments:

Reviewer #1 (Remarks to the Author)

In this study, Wang and coworkers present a novel NIR-II fluorescent nanosensor for real-time, non-destructive monitoring of H_2O_2 signaling in living plants, demonstrating its impressive sensitivity and species-independence as a reliable means for the real-time report of stress information. Further, the integration with machine learning model for stress classification further highlights its potential in precision agriculture. Overall, the reviewer finds the present study is well organized and possesses certain innovation and practical application value. I believe major revisions are required before this manuscript can be finally published.

[Author Response]: We would first like to thank the reviewer for the positive comment on the significance and quality of our work. Your insightful comments have been invaluable in improving our work. We have tried our best to revise our manuscript accordingly. Below, we address each comment point by point, and the specific changes made to the manuscript in response to each point are highlighted in ***yellow***.

[Reviewer 1 comment 1] In the introduction, it is necessary to elaborate on the unique advantages and core contributions of the proposed nanosensor compared to existing NIR-II fluorescence-based technologies. For example, (i) how does the performance of the proposed sensor compared to other state-of-the art NIR-II sensors in terms of sensitivity, selectivity, and real-time response capability? As known, the synthesized NIR-II molecular probe in this work is already reported and characterized by Tang and coworkers, Nature Communications 11, 1255 (2020), J. Am. Chem. Soc. 2019, 141, 13, 5359.

[Author Response]: We would like to thank the reviewer for this constructive comment. Compared to existing NIR-II fluorescence-based technologies, our proposed nanosensor offers unique advantages. The nanosensor features an innovative design that integrates stable AIE fluorophores with H_2O_2-sensitive POMs, achieving exceptional performance in terms of sensitivity, selectivity, and real-time response capability.

In terms of sensitivity, AIE_{1035}NPs@Mo/Cu-POM exhibits a detection limit of 0.43 μM, which is better than or comparable to most NIR-II sensors (Supplementary Table 2). Plant stresses, including drought, salinity, chilling, heat shock, heavy metals, and ultraviolet radiation, can disrupt cellular homeostasis, leading to the generation of H_2O_2 at levels exceeding 5 μM (*Trends Plant Sci.* 7, 405-410 (2002))[1]. Therefore, the detection sensitivity of AIE_{1035}NPs@Mo/Cu-POM is adequate for detecting the physiological concentrations of H_2O_2 produced by plants under stress conditions.

In terms of selectivity, we found that interference from plant hormones, reducing agents, metal ions, and other active compounds had minimal impact on the nanosensor (Supplementary Fig. 19a). Although various ROS induced different degrees of fluorescence intensity increases *in vitro*, the nanosensor exhibited a high selectivity for H_2O_2 *in vivo* (Supplementary Fig. 19b-d). This selectivity may be attributed to the longer lifetime of H_2O_2, which ranges from milliseconds to seconds, compared to other ROS in the plant biological environment (*Nat. Immunol.* **3**, 1129-1134 (2002))[2]. •OH, $^1O_2$, and $O_2^{\bullet-}$ are rapidly decomposed and scavenged within plant cells, and their short half-lives on the order of microseconds, may be shorter than the sensor's response time for detecting these transient molecules (*New Phytol.* **221**, 1197-1214 (2019)[3]; *Nat. Plants.* **6**, 404-415 (2020)[4]). Therefore, the NIR-II nanosensor can specifically monitor the dynamics of H_2O_2 in plants.

Regarding **real-time response capability**, the proposed nanosensor exhibits rapid binding kinetics. Upon the addition of H_2O_2, NIR-II fluorescence emission rapidly recovered within 1 min (Supplementary Fig. 17), implying that dynamic biological processes can be monitored in real-time and continuously. This real-time response capability represents a significant advantage over previous NIR-II sensors, which typically require prolonged incubation times ranging from tens of minutes to hours (Supplementary Table 2). Consequently, the NIR-II nanosensor is well-suited for real-time monitoring of H_2O_2 dynamics.

Regarding **photostability**, under constant laser beam irradiation, the signal intensity of AIE_{1035}NPs exhibited remarkable stability. In contrast, indocyanine green (ICG) showed a decline in signal intensity, highlighting the advantages of AIE_{1035}NPs for the

continuous monitoring of biological information in plants (Fig. 2h).

To further emphasize these points, we have revised the introduction to compare the performance of our nanosensor with other state-of-the-art NIR-II sensors. Additionally, we have included specific data (Supplementary Table 2) to support our claims regarding sensitivity, selectivity, and real-time response capability. The revised content is as follows:

"The sensor's sensitivity of 0.43 μM and response time of 1 min surpass those of existing NIR-II sensors, enabling rapid, real-time monitoring of trace levels of H_2O_2." (Page 4-5, line 72-74 in revised manuscript)

Supplementary Table 2. Comparison of the sensing performance of different fluorescence probes for the detection of H_2O_2.

Probe	Detection window	Peak emission wavelength (nm)	Linear range (μM)	LOD (μM)	Selectivity	Response time (plateau reached)	Ref/ Year
HYL	NIR-I	723	10-70	2.76	Good for 16 biological interferences	150 min	[5]/2023
HCy-H_2O_2	NIR-I	720	1-200	0.53	Good for 32 biological interferences	15 min	[6]/2024
BTPE-NO_2@F127	NIR-II	938	0-10	0.74	Good for 12 biological interferences	60 min	[7]/2021
GNP-KTP5-ICG	NIR-II	810	30-100	16.2	-	-	[8]/2021
Ag/Ag_2S JNPs	NIR-II	1250	10-5×10^4	10	Good for 5 ROS and metal ions	24 h	[9]/2021
Nd@POM	NIR-II	1060	0.5-3	0.15	Good for 15 biological interferences	2 min	[10]/2023
BX-BOH@BSA	NIR-II	938	-	0.77	Good for 13 biological interferences	80 min	[11]/2023
HRP-SWCNT	NIR-II	1135	150-600	31	Good for 3 relevant analytes	30 min	[12]/2024
AIE_{1035}NPs@ Mo/Cu-POM	NIR-II	1035	1-40	0.43	Good for 7 compounds commonly found in plants	1 min	This work

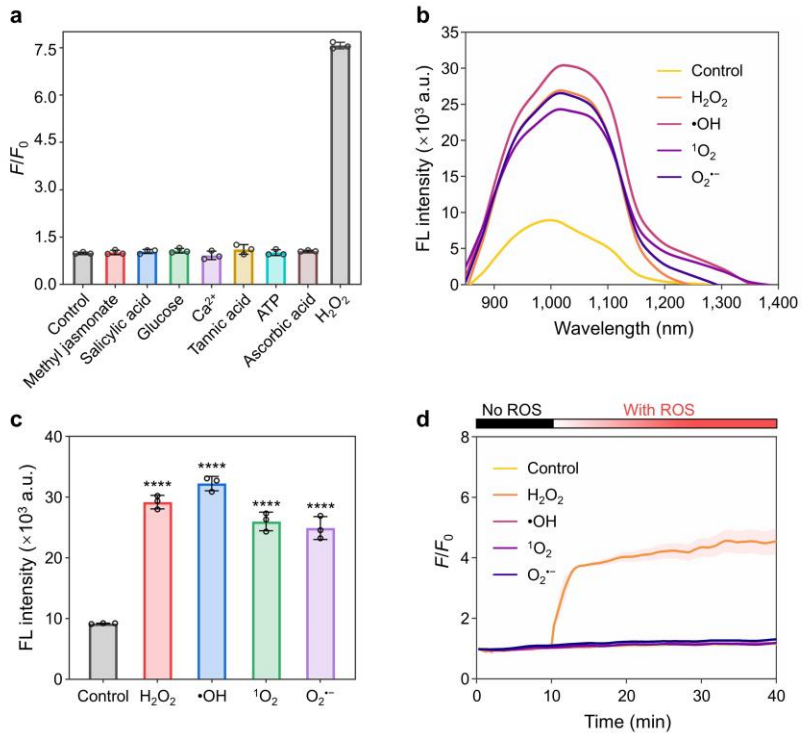

Supplementary Fig. 19. Fluorescence intensity of the nanosensor in response to ROS and various compounds commonly found in plants. (a) Fluorescence intensity at 1035 nm of AIE$_{1035}$NPs@Mo/Cu-POM in response to H_2O_2 and other molecules typically involved in plant systems. Laser excitation: 808 nm, 15 mW. Filter: 850 nm long-pass filter. Data are presented as mean ± s.d. from three independent measurements and the corresponding data points are presented as open circles. (b) Fluorescence spectra of nanosensors after reaction with ROS. (c) Fluorescence intensity at 1035 nm of AIE$_{1035}$NPs@Mo/Cu-POM response to ROS. Data are mean ± s.d. from three independent experiments. Statistically significant differences were determined using two-tailed unpaired t-test. The asterisks indicate values that are significantly different from the control (****P < 0.0001). (d) *In vivo* nanosensor response to ROS infiltration on a lettuce leaf. Dose-responses relationships are illustrated by the relative fluorescence intensity of AIE$_{1035}$NPs@Mo/Cu-POM upon the infiltration of ROS (100 μM). Shaded regions represent the standard error across three independent measurements.

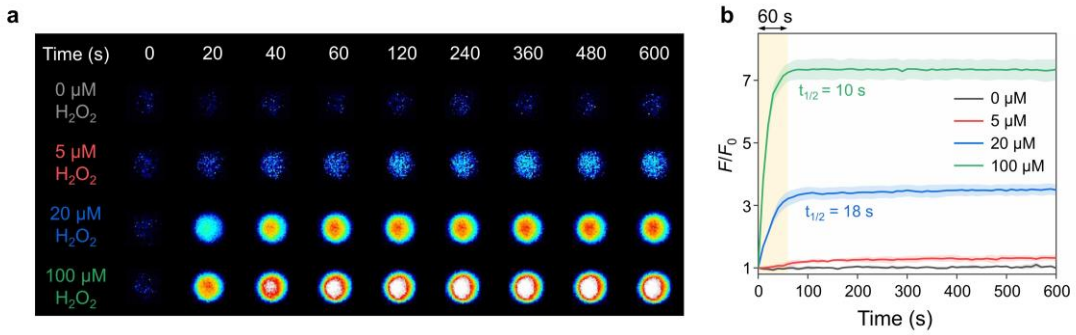

Supplementary Fig. 17. Evaluation of the nanosensor response time. (a) NIR fluorescence images of AIE$_{1035}$NPs@Mo/Cu-POM after reaction with H_2O_2. Laser excitation: 808 nm, 15 mW. Filter: 900 nm long-pass filter. (b) Reaction kinetics between AIE$_{1035}$NPs@Mo/Cu-POM and H_2O_2. The half-life of the reaction was calculated to be 18 s and 10 s for 20 μM H_2O_2 and 100 μM H_2O_2, respectively. The reaction was completed within 60 s. Shaded regions represent the standard error across three independent measurements.

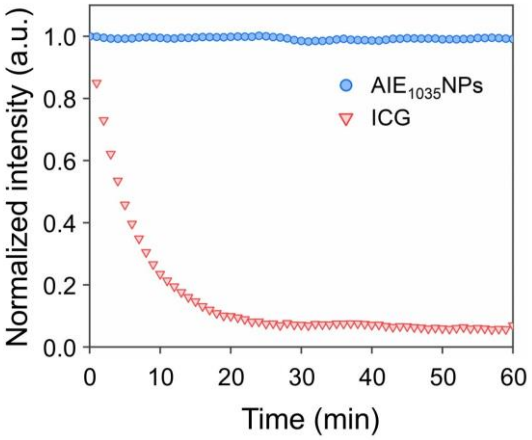

Fig. 2h. Photostability evaluation of the AIE$_{1035}$NPs dispersion and ICG solutions under constant laser beam exposure for 60 min. Laser excitation: 808 nm, 100 mW.

The NIR-II molecule used in this work shares significant structural similarities to the AIE molecules previously reported by Tang and coworkers. All of these molecules adopt a donor-acceptor-donor (D-A-D) architecture, featuring tritylene amine (TPA) as the electron-donating unit and benzo[1,2-c:4,5-c′]bis[1,2,5]thiadiazole (BBTD) as the strong electron-accepting core. A common design strategy among these molecules involves the introduction of spatial hindrance to enforce a twisted molecular conformation, which reduces intermolecular interactions while facilitating

intramolecular motions. This twisted configuration is essential for promoting twisted intramolecular charge transfer (TICT) and achieving AIE characteristics.

The NIR-II molecule developed in this study incorporates an alkyl thiophene moiety that is distinct from those used in previously reported AIE structures (Reviewer-only Fig. 1). To evaluate the AIE effect of this molecule, water was gradually introduced into the solvent system, increasing the volume fraction (f_w) from 0 to 90% (Supplementary Fig. 1a-c). The fluorescence intensity of AIE_{1035} enhanced remarkably, owing to the restriction of intramolecular motion mechanism triggered by aggregate formation. According to previous works, the α_{AIE} is defined as the ratio of the PL intensity at f_w = 90% to that at f_w = 0%. AIE_{1035} exhibited an α_{AIE} of 7.9, which differs from the previously reported molecules 2TT-*o*C26B (10.8), 2TT-*o*C610B (6.9), and 2TT-*o*C6B (6.0). We hypothesize that the differences in emission properties in the aggregate state arise from the different alkyl chains in these molecules. Compared to 2TT-*o*C6B, 2TT-*o*C26B and AIE_{1035}, with their larger alkyl chains, exhibit more twisted structures, which help to mitigate detrimental intermolecular interactions in the aggregate.

To further emphasize the advantages of this common structure, we have revised the manuscript to introduce and summarize the design strategy of the AIE fluorophores used in this work, alongside similar fluorophores reported previously (*Nat. Commun.* 11, 1255 (2020)[13], *J. Am. Chem. Soc.* 2019, 141, 13, 5359[14]). This revision aims to highlight the advantages of the selected AIE fluorophores in molecular engineering design. The revised content is as follows:

"This design features a strong donor-acceptor-donor (D-A-D) molecular structure, incorporating rotating units and π-conjugated bridges that introduce specific spatial hindrance. The strong electron-withdrawing group benzo[1,2-c:4,5-c′]bis[1,2,5]thiadiazole (BBTD) serves as the acceptor unit with a quinoidal structure, which facilitates greater electron delocalization and consequently reduced the bandgap[14]. The donor units trimethylamine (TPA), acts as molecular rotors in AIE_{1035}, ensuring the intramolecular rotation. TPA's strong electron-donating capability and larger molecular structure inhibit intermolecular interactions in the aggregated state. The planar thiophene ring acts both as a secondary donor group and a π-conjugated unit,

facilitating the intramolecular charge transfer (ICT) from TPA to BBTD. The branched carbon alkyl chains on the thiophene provide tunable steric hindrance, preventing excessive aggregation[13]." (Page 5-6, line 92-102 in revised manuscript)

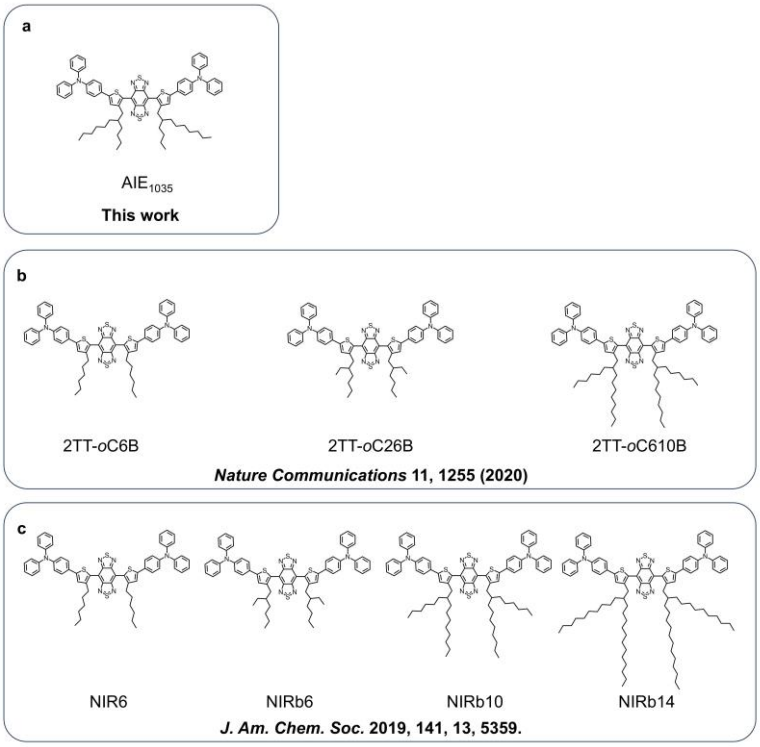

Reviewer-only Fig. 1 | The molecular structural formulae of AIE used in this work and reported previously.

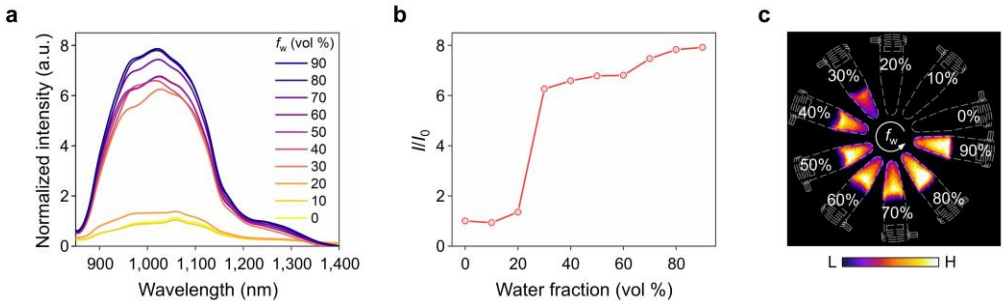

Supplementary Fig. 1. Validation of the AIE effect. (a) Normalized NIR fluorescence spectra of AIE_{1035} (10 μM) in the tetrahydrofuran/water mixtures with different water volume fractions (f_w). Laser excitation: 808 nm, 15 mW. Filter: 850 nm long-pass filter. (b) Plots of the relative emission intensity (I/I_0) versus f_w, where I_0 and I represent the fluorescence peak values of AIE_{1035} in the tetrahydrofuran and tetrahydrofuran/water mixtures, respectively. (c) NIR fluorescence images of AIE_{1035} (10 μM) in tetrahydrofuran/water mixtures with different f_w. Laser excitation: 808 nm, 15 mW. Filter: 900 nm long-pass filter.

[Reviewer 1 comment 2] (ii) Considering the fact that NIR-II imaging is widely utilized in precision medical diagnosis and treatment, when the application scenario switches to plants stress monitoring, what are the similarities and differences between them, such as depth of penetration or fluorescence wavelengths and etc.

[Author Response]: NIR-II imaging, known for its deep tissue penetration, low autofluorescence, and high signal-to-noise ratio (SNR), has been extensively researched for its applications in precision medical diagnosis and treatment. When adapting this imaging technique for plant stress monitoring, NIR-II imaging can similarly capitalize on these advantages. However, differences emerge due to the unique structural and biochemical properties of plant tissues.

In both biomedical and plant applications, NIR-II imaging utilizes a variety of fluorescent nanomaterials to facilitate deep-tissue visualization and physiological monitoring. In biomedical imaging, the deep tissue penetration of NIR-II fluorescence enables the visualization of blood vessels, tumors, and other internal structures, typically aided by exogenous contrast agents such as quantum dots, rare-earth doped nanoparticles, or organic fluorophores. In plant stress monitoring, NIR-II fluorescent nanomaterials (often carbon nanotubes and organic fluorophores) are utilized to monitor physiological changes in response to both abiotic and biotic stresses, particularly in tissues such as leaves and roots.

The penetration depth of NIR-II fluorescence differs in animal and plant tissues. In animal soft tissues, penetration can reach several millimeters to centimeters, while in plant tissues, due to the dense cellular structure, penetration is generally limited to sub-millimeter to millimeter depths. We compared the imaging performance of NIR-II fluorescent materials in both animal and plant tissues using AIE_{1035}NPs with an emission wavelength of 1035 nm (Reviewer-only Figs. 2-3). Imaging experiments were conducted on 1% Intralipid, plant extract, chicken breast, and lettuce leaves. 1% Intralipid was selected as a tissue model being similar to those of biological tissues. A glass capillary tube filled with an aqueous solution of AIE_{1035}NPs was placed under a cylindrical culture dish and covered with different volumes of 1% Intralipid or plant extract. An 808 nm laser and a 900 nm long-pass filter were used, and the imaging

conditions were kept consistent. Reviewer-only Fig. 2 showed that the strong light scattering in 1% Intralipid interfered with fluorescence signals, thereby reducing the SNR of the imaging. The light scattering effect in the plant extract was relatively less pronounced than that in 1% Intralipid, resulting in improved NIR-II fluorescence imaging with a higher SBR. In imaging experiments with chicken breast and lettuce leaves, the NIR-II fluorescence signal inevitably decreased as the thickness of the coverage increased (Reviewer-only Fig. 3).

In biomedical applications, most fluorescent biomolecules show emissions in the visible window. For example, the pyridine nucleotides found in DNA and RNA, aromatic amino acids such as tryptophan, energy transporters like nicotinamide adenine dinucleotide, flavins, and structural proteins such as collagen and elastin exhibit fluorescence (*Nat. Rev. Bioeng.* **1**, 60-78 (2023))[15]. Autofluorescence decreases when the imaging wavelength is extended into the NIR window. In plant imaging, compounds such as flavonoids and chlorophyll produce significant background fluorescence interference in the visible and NIR-I regions, making NIR-II probes more suitable for monitoring stress. We collected imaging data for chicken breast and chili pepper leaves in the visible (430 nm excitation), NIR-I (605 nm excitation), and NIR-II (808 nm excitation) regions (Reviewer-only Fig. 4 and Supplementary Fig. 22). Visible and NIR-I imaging was performed using the IVIS Spectrum imaging system in fluorescence mode, with excitation wavelengths of 430 nm or 605 nm and emission wavelengths ranging from 500 nm to 840 nm. NIR-II imaging was carried out using a home-built NIR-II imaging system with an 808 nm excitation wavelength and various long-pass filters. In Reviewer-only Fig. 4, chicken breast exhibited weak or negligible autofluorescence in the imaging windows. In Supplementary Fig. 22, the leaves exhibited varying degrees of autofluorescence in the visible and NIR-I regions, particularly in the NIR-I region, where the fluorescence signal was enhanced due to the inherent presence of chlorophyll. Similarly, both chicken breast and pepper leaves showed very low autofluorescence in the NIR-II region. Therefore, NIR-II imaging, with its superior penetration depth and minimal autofluorescence, facilitates high-resolution imaging of physiological changes in both animals and plants.

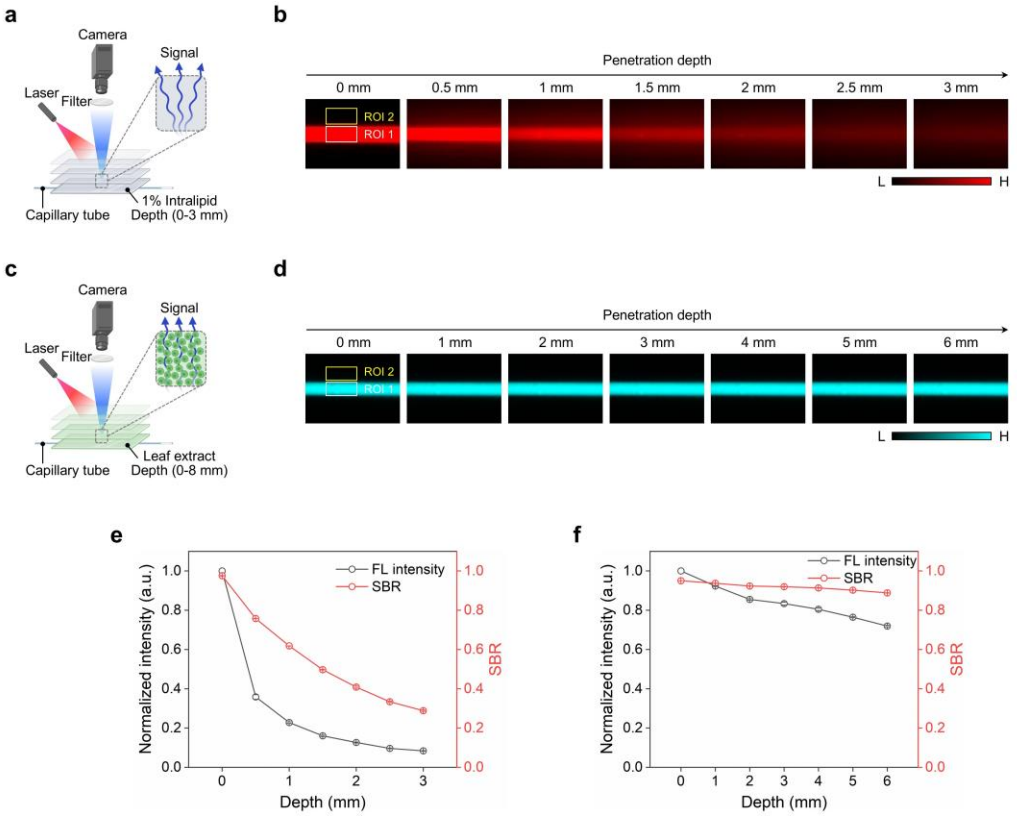

Reviewer-only Fig. 2 | Imaging of NIR-II AIE$_{1035}$NPs in 1% Intralipid and plant extracts. Schematic illustration of the investigation of deep penetration in 1% Intralipid (a) and plant extracts (c). Fluorescence images of capillaries with 0 mm-3 mm 1% Intralipid (b) and 0 mm-6 mm plant extracts (d) covered. Normalized SBR (defined as (ROI1 − ROI2)/ROI1) of capillary images in fluorescent channel obtained for different volumes of 1% Intralipid (3) and plant extracts (f) covered. The bars represent mean ± SD derived from n = 3 replicate analysis results.

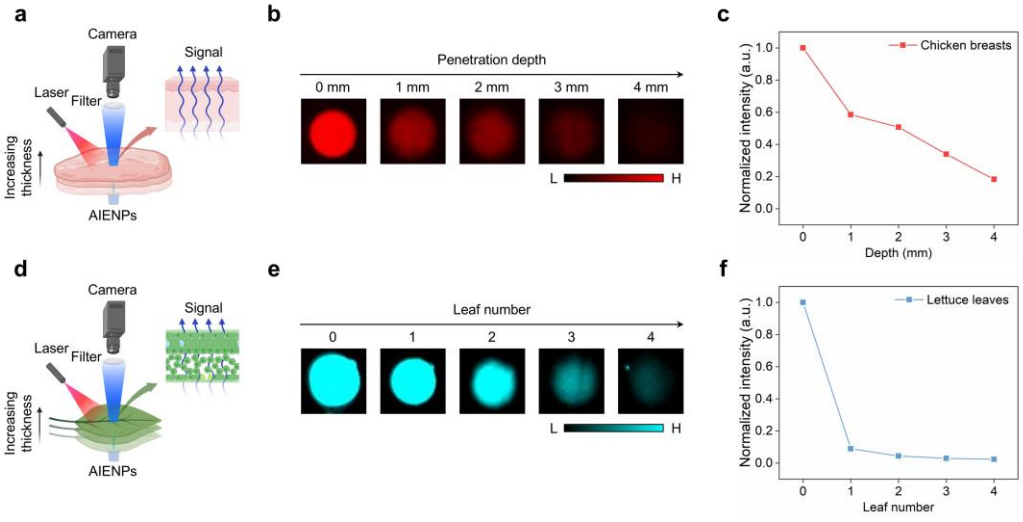

Reviewer-only Fig. 3 | Imaging of NIR-II AIE$_{1035}$NPs in chicken breast and lettuce leaves. Schematic illustration of the investigation of deep penetration in chicken breast

(a) and lettuce leaves (d). Fluorescence images of AIE_{1035}NPs-filled 96-well plates through stacked chicken breast (b) and pepper leaves (c). Corresponding normalized fluorescence intensity of AIE_{1035}NPs with stacked chicken breast (c) and pepper leaves (f) in (b) and (e).

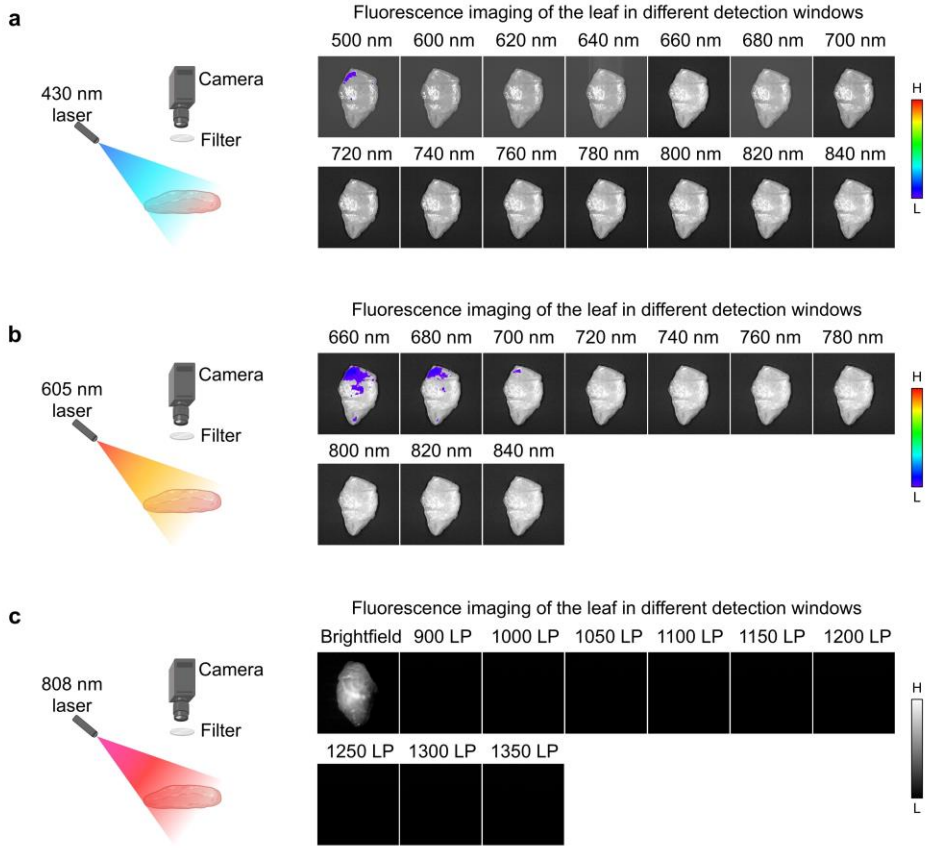

Reviewer-only Fig. 4 | Chicken breast autofluorescence at various laser wavelengths. Fluorescence images of chicken breast under laser excitation at 430 nm (a), 605 nm (b), and 808 nm (c). The chicken breast autofluorescence in images (a) and (b) was acquired using different detection windows (500 ± 10, 600 ± 10, 620 ± 10, 640 ± 10, 660 ± 10, 680 ± 10, 700 ± 10, 720 ± 10, 740 ± 10, 760 ± 10, 780 ± 10, 800 ± 10, 820 ± 10, and 840 ± 10 nm) by an IVIS Spectrum platform. The chicken breast autofluorescence in images(c) was acquired using a home-built NIR imaging system equipped with various long-pass optical filters.

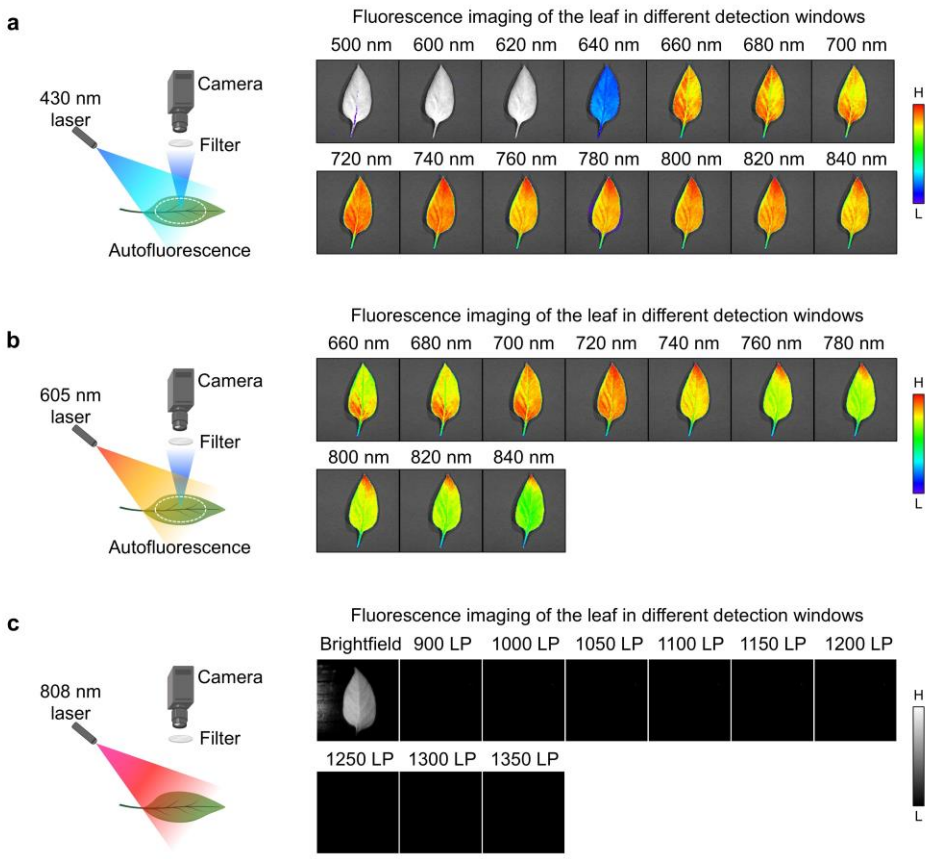

Supplementary Fig. 22 | Leaf autofluorescence at various laser wavelengths. Fluorescence images of the pepper leaf under laser excitation at 430 nm (a), 605 nm (b), and 808 nm (c). The leaf autofluorescence in images (a) and (b) was acquired using different detection windows (500 ± 10, 600 ± 10, 620 ± 10, 640 ± 10, 660 ± 10, 680 ± 10, 700 ± 10, 720 ± 10, 740 ± 10, 760 ± 10, 780 ± 10, 800 ± 10, 820 ± 10, and 840 ± 10 nm) by an IVIS Spectrum platform. The leaf autofluorescence in images (c) was acquired using a home-built NIR imaging system equipped with various long-pass optical filters.

[Reviewer 1 comment 3] In addition, while the manuscript emphasizes the sensor's broad applicability to various plant species, it would be valuable to discuss whether its detection sensitivity or specificity surpasses that of previously reported methods.

[Author Response]: We would like to thank the reviewer for raising this important point. In the manuscript, we emphasize the broad applicability of our nanosensor across various plant species, highlighting its potential for use in different plant systems. Regarding the sensor's detection sensitivity and specificity, we have compared its performance with previously reported methods and found that it offers distinct

advantages.

In the revision, we have included a comprehensive comparison table (Supplementary Table 2) that summarizes the detection window, peak emission wavelength, detection linear range, LOD, selectivity, and response time of our sensor in comparison to previously reported sensors. Additionally, we compared the most important properties (sensitivity and response time) of the proposed nanosensor with other state-of-the-art NIR-II sensors in the introduction section. The revised content is as follows:

"The sensor's sensitivity of 0.43 μM and response time of 1 min surpass those of existing NIR-II sensors, enabling rapid, real-time monitoring of trace levels of H_2O_2."

(Page 4-5, line 72-74 in revised manuscript)

In addition, we have integrated various detection methods for H_2O_2 in plants, including molecular probes, nanoprobes, genetically encoded probes, and electrochemical probes, as detailed in Supplementary Table 4. Through these comparative analyses, we aim to elucidate the advantages of the NIR-II nanosensor, which include reduced background interference, rapid and sensitive response, non-invasive detection, and broad applicability across different plant species. We have included these comparisons in the revised supporting information.

Supplementary Table 4. Representative sensors for detecting plant molecules associated with stress.

Sensing method	Analytes	Materials	Size	Plant species	Localization	Stress	LOD	Linear range	Refs
Optical	H_2O_2	H_2DCFDA	-	*Arabidopsis thaliana*	Whole plants	Light, wounding, pathogen	-	-	16
Optical	H_2O_2	2E2F	-	Malus hupehensis seedlings, 'Orin' apple calli, *Nicotiana benthamiana*	Calli, leaves	Wounding, high salinity, high light, drough	-	10-100 μM	17
Optical	H_2O_2	CT-XA-H_2O_2	-	Soybean, peanut	Sprouts	Cd^{2+}, high salinity	-	0-100 μM	18
Optical	H_2O_2	IXD-B	-	Mung bean, okra	Sprouts	Cd^{2+}	-	0-180 μM	19
Optical	H_2O_2	7,6 ss$(GT)_{15}$ SWCNT 6,5 ss$(AT)_{15}$ SWCNT	-	*Arabidopsis thaliana*	Leaves	-	-	-	20
Optical	H_2O_2	G-SWNT, A-SWNT	3.1 ± 0.1 nm (diameter) 613 ± 15 nm (length)	Lettuce, arugula, spinach, strawberry blite, sorrel, *Arabidopsis thaliana*	Leaves	Wounding, flg22, high light, high heat	55.7 μM (K_d)	-	4

Optical	H_2O_2	HeAptDNA-SWCNT	-	*Arabidopsis thaliana*	Leaves	UV-Blight, high light, flg22, wounding	-	0-1000 μM	21
Optical	H_2O_2	C_{20}/AgNC, FAM-C_{20}/AgNCs-Cy5	-	*Arabidopsis thaliana*, *Nicotiana benthamiana*	Roots, leaves	Pathogen	-	-	22
Optical	H_2O_2	AIE_{1035}NPs@Mo/Cu-POM	230 nm	*Arabidopsis thaliana*, lettuce, spinach, pepper, tobacco.	Leaves	Wounding, flg22, high heat	0.43 μM	1-40 μM	This work
Genetically encoded protein	H_2O_2	Hyper2	-	*Nicotiana benthamiana*	Whole plants	High light	-	-	23
Genetically encoded protein	H_2O_2	Hyper7	-	*Arabidopsis thaliana*	Whole plants	Pathogen, laser light	-	-	24
Genetically encoded protein	H_2O_2	roGFP2-Orp1	-	*Arabidopsis thaliana*	Whole plants	Pathogen	-	-	25
Electrochemical	H_2O_2	Nano-Au/ss	100 μm	Tomato	Stems	High salinity	3.97 μM	10-1000 μM	26
Electrochemical	H_2O_2	Hb/SWCNTs/CFUME	7 μm	Aloe	Leaves	High salinity	4 μM	4.90-405 μM	27
Electrochemical	H_2O_2	Nafion/Pt	1000 μm	Oilseed rape	Stems	Drought	1.24 μM	≤ 0.3mM	28
Electrochemical	H_2O_2	AuNPs/ITO	20 mm × 8 mm	Tomato	Leaves	Pathogen	-	0-1000 μM	29

[Reviewer 1 comment 4] Regarding the dataset used for the machine learning model, it is recommended to include details on its composition in the main text. Information such as the distribution of fluorescence intensity levels, stress conditions, and plant species within the dataset would provide a clearer understanding of its structure. Furthermore, the potential effects of class imbalance or dataset heterogeneity on the model's accuracy should be analyzed. The criteria for selecting these species and their relevance to the broader scope of stress response studies should be further clarified.

[Author Response]: We would like to thank the reviewer for this valuable suggestion. In our study, the dataset used for the ML model consists of nanosensor fluorescence intensity data collected from lettuce under various stress conditions, including no stress, flg 22, heat, and wounding. Additionally, we have incorporated ML models from different plant species (tobacco, lettuce, spinach, and pepper) responding to the same stress condition (wounding) in the revised manuscript. We have provided a schematic representation of the ML architecture in Fig. 6a and heat maps illustrating fluorescence changes in nanosensors monitoring different types of stress and plant species in Fig. 6b. We have included a more detailed description of the dataset in the revised main text. The revised content is as follows:

"To evaluate the effectiveness of AIE_{1035}NPs@Mo/Cu-POM in monitoring stress responses, controlled experiments were conducted on lettuce plants using four

experimental conditions: no stress, flg22 treatment, heat stress, and mechanical wounding. Additionally, mechanical damage treatment was applied to different plants, including tobacco, lettuce, spinach, and pepper. The site of probe injection in each plant served as a fixed location for signal extraction, and the NIR-II signal was continuously recorded and automatically extracted for one hour to generate the raw time series data. All signals were calibrated and normalized to ensure that the features extracted after data preprocessing were applicable to the overall dataset (Fig. 6a). Cellular homeostasis is characterized by a baseline level of ROS, which can be disrupted by various biotic and abiotic stresses, leading to ROS accumulation in different cellular compartments[30]. For each stress condition, the NIR-II signals of the nanosensors exhibited significant variation in response to each stressor (Fig. 6b). In the control experiment without stress, the fluorescence signal of the nanosensor remained relatively stable over the course of one hour, as H_2O_2 was present at a lower concentration and was scavenged by a range of enzymatic and non-enzymatic antioxidants[31]. During the wounding experiments, the disruption of leaf tissue triggered a rapid accumulation of H_2O_2, leading to pronounced changes in the NIR-II fluorescence signal. Under heat stress, when membrane complexes involved in various electron transfer chains are compromised, H_2O_2 is produced in mitochondria and chloroplasts, subsequently accumulating in the cytoplasm and nucleus[32]. The signal changes observed in the nanosensor were consistent with immediate physiological responses of the plants. In the flg22-simulated pathogen stress experiments, H_2O_2 is primarily produced in the apoplast due to the activation of specific oxidases such as RBOHs, as well as in chloroplasts due to the disruption and imbalance of metabolic pathways[33,34], which leads to an increase in the signal of the NIR-II nanosensor. During the wounding experiments across different plant species, each species showed distinct characteristic H_2O_2 signaling responses, which aligns with the heterogeneity of the characteristic parameters of the H_2O_2 signaling waves observed in the four species previously studied (Supplementary Fig. 42), indicating the diversity of the signaling networks utilized by these plant species. These results indicat that the proposed NIR-II fluorescent nanosensor can effectively monitor stress-induced H_2O_2 signaling in real-time." (Page 15-16, line 293-320 in

revised manuscript)

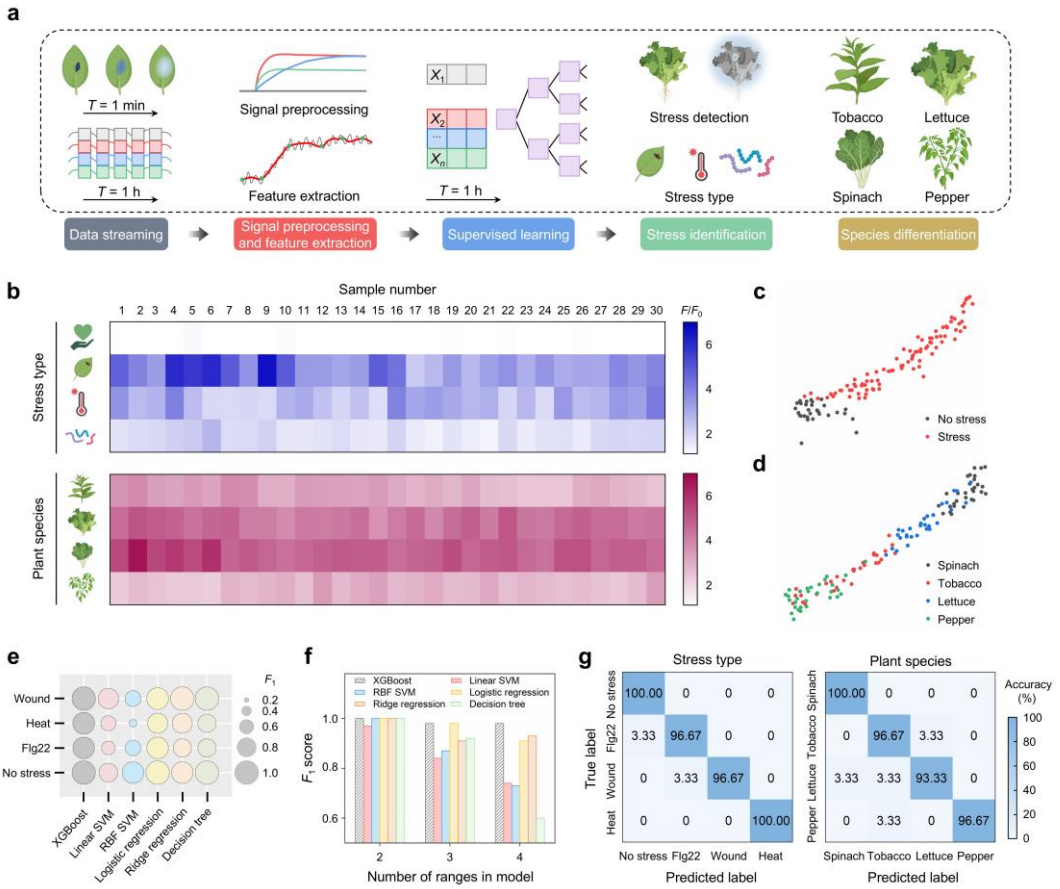

Fig. 6 | ML-powered plant stress status monitoring. a, Schematic of the ML architecture for signal preprocessing, feature extraction, supervised learning, stress identification, and species differentiation. **b,** Heat maps of fluorescence changes in nanosensors monitoring different stress types and plant species over an hour. The intensity levels represent the changes in F/F_0 of nanosensors in lettuce leaves under different stress conditions, including no stress, wound, heat, and flg22 treatment (top panel), as well as in response to mechanical damage across different plant species, including tobacco, lettuce, spinach, and pepper leaves (bottom panel). **c, d,** t-distributed stochastic neighbour embedding plots for the no stress and stress datasets (**c**) and different species stress datasets (**d**). Visual clustering results showed the feature separation in two-dimensional space. **e,** F_1 scores (a metric of accuracy combing precision and recall) of different ML models for stress classification. **f,** F_1 scores of different ML models across an increasing number of ranges categorized by stress identification. The ranges of stress classification include 2 ranges (no stress/stress), 3 ranges (no stress/biotic stress/abiotic stress), and 4 ranges (no stress/flg22/wound/heat). **g,** Confusion matrices of an XGBoost model displaying the classification accuracy for

predicting each type of stress and different plant species.

In our dataset, the number of stressed conditions exceeds that of unstressed conditions, and abiotic stress conditions outnumber the biotic stress conditions. Relying solely on accuracy can result in a misleading interpretation of high results. Therefore, we introduce several metrics to evaluate the performance of machine learning models. For stress identification tests, we used confusion matrix, accuracy, and F_1 score. For species differentiation tests, the confusion matrix was used for ML evaluation.

Confusion matrix is a table that visualizes the accuracy of of predictions by comparing actual classes to predicted classes (Fig. 6g and Supplementary Fig. 45b). In binary classification, the confusion matrix consists of two classes: positive and negative. True positive (TP) occurs when a prediction correctly identifies the positive class, while true negative (TN) occurs when a prediction accurately identifies the negative ones. False positive (FP) arises when a prediction incorrectly identifies the positive class, and false negative (FN) occurs when a prediction incorrectly identifies the negative class. In multiclass classification, the confusion matrix includes all labeled classes. Accuracy is defined as the total number of correct predictions divides by the total number of predictions, and it can be expressed mathematically as follows:

$$\text{Accuracy} = \frac{\text{TP} + \text{TN}}{\text{TP} + \text{TN} + \text{FP} + \text{FN}}$$

However, accuracy may not be an appropriate measure when the dataset is imbalanced. A high accuracy in the majority class may lead to an overall high accuracy for the model, even if the predictions for other classes are poor. In our dataset, the stressed conditions outnumber the unstressed conditions, and abiotic stress conditions outnumber the biotic stress conditions. Relying solely on accuracy can result in a misleading interpretation of high performance. Therefore, we introduce the F_1 score, a combination metric derived from precision and recall (Fig. 6e, f and Supplementary Fig. 45b). Precision measures the relevance of the results, while recall assesses how many truly relevant results are returned. Theses metrics are defined as follows:

$$\text{Precision} = \frac{\text{TP}}{\text{TP} + \text{FP}}$$

$$\text{Recall} = \frac{\text{TP}}{\text{TP} + \text{FN}}$$

The stress identification models were evaluated using the F_1 score, averaged over the different iterations of cross-validation. The F_1 score is a metric that assesses the accuracy of the model by combining precision and recall, and is defined as follows:

$$F_1 \text{ score} = 2 \times \frac{\text{Precision} \times \text{Recall}}{\text{Precision} + \text{Recall}}$$

In addition, we applied Random Undersampling, a widely used technique for addressing class imbalance, to improve the learning performance of the minority class within the model. Random Undersampling alleviates class imbalance by randomly removing samples from the majority class, thereby achieving a more balanced distribution of samples across classes. Random Undersampling was performed on both the 2 ranges classification stress dataset and the 3 ranges abiotic stress dataset (Supplementary Fig. 46). We found that after Random Undersampling, the 2 ranges and 3 ranges datasets formed distinct clusters in t-distributed stochastic neighbor embedding (t-SNE) plots (Supplementary Fig. 46a, b), indicating that the class imbalance did not adversely affect the clustering structure of H_2O_2 signals induced by different stresses. Utilizing the XGBoost model, we were still able to predict stress species with a limited number of samples in the training dataset, achieving relatively high accuracy and F_1 scores (Supplementary Fig. 46c, d). We have added the relevant analysis in the revised supporting information (Supplementary Note 20: ML evaluations and metrics).

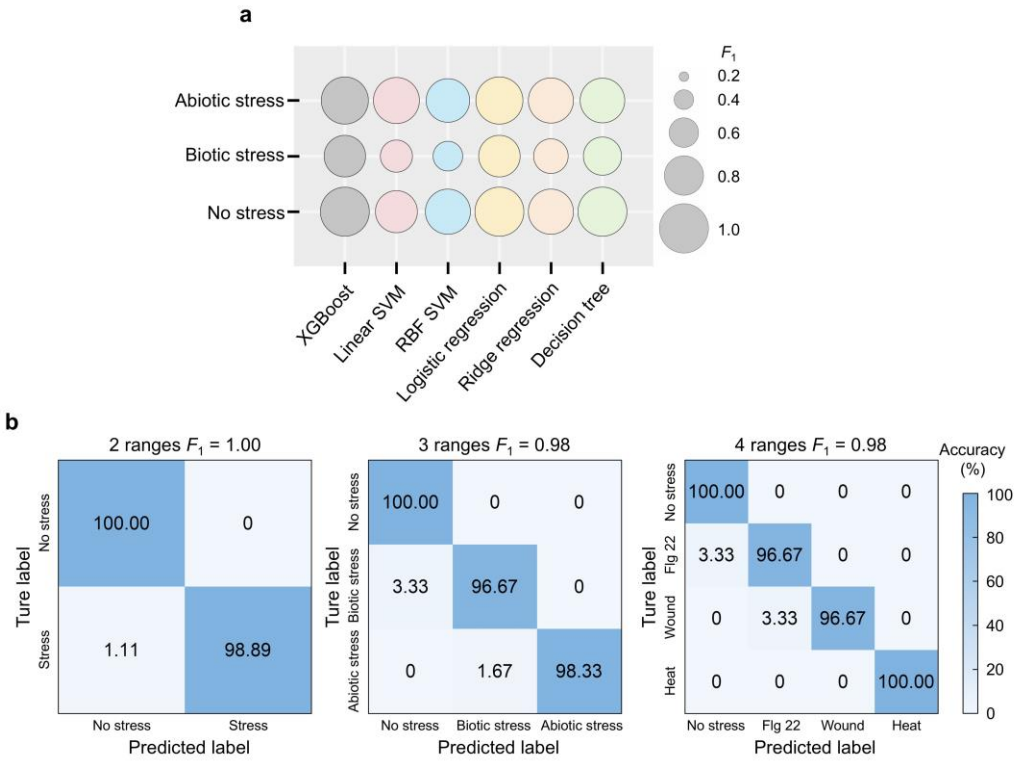

Supplementary Fig. 45. Performance of ML models in predicting stress detection. a, F_1 scores for various ML models used in stress classification. b, Confusion matrix for the XGBoost model illustrating the classification accuracy and F_1 scores for predicting no stress/stress (2 ranges) model, categorization of biotic stress and abiotic stress (3 ranges) model, and identification of specific stress species (4 ranges) model.

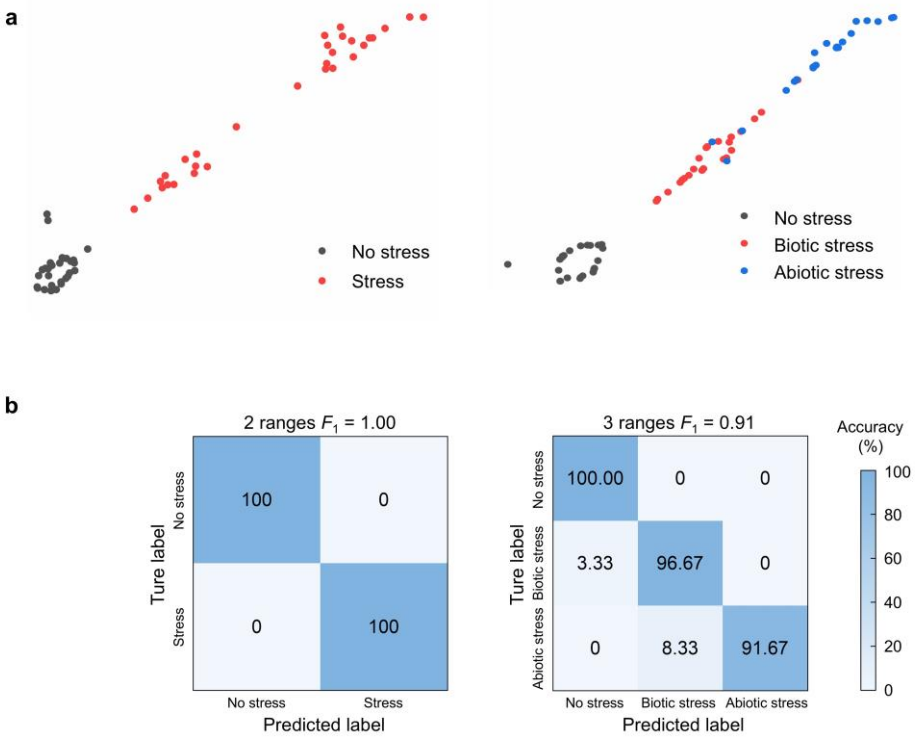

Supplementary Fig. 46. Performance of ML after Random Undersampling. a, t-SNE plots for 2 ranges and 3 ranges datasets processed using Random Undersampling. b, Confusion matrix of the XGBoost model displaying the classification accuracy and F_1 score for predicting no stress/stress (2 ranges) model and the categorization of biotic stress and abiotic stress (3 ranges) model after Random Undersampling.

During the monitoring of plant signaling waves, we recognized the significance of species selection criteria in broader studies of stress responses. The selected plant species exhibit a range of metabolic characteristics and levels of stress tolerance, including a model plant (tobacco) and non-model plants (lettuce, spinach, and pepper). Over the past few decades, the increasing interest in low-calorie diets has led to an increased demand for lettuce and spinach. With a cultivated area of 880,000 hectares, lettuce is a commercially significant crop with the highest total production among all vegetables[35]. Global spinach production is approximately 30.1 million tons per year, encompassing both fresh and processed markets (frozen and canned)[36]. As common leafy vegetables, lettuce and spinach play a crucial role in agricultural production and are highly susceptible to various environmental stresses. Studying their stress responses can help optimize cultivation conditions, improve yields, and enhance quality. Tobacco, one of the most economically significant crops, has long been used for both medicinal and recreational purposes by human societies. In fact, cultivated tobacco (*N. tabacum*) is among the most chemically and biologically well-studied species in the plant kingdom and was the first plant to be genetically modified[37]. The wild tobacco species *N. benthamiana* has been an important model in research on plant−pathogen interactions and molecular biology. The K326 variety used in this study is a widely cultivated type of roasted tobacco, known for its excellent agronomic traits and high-quality quality. Investigating the stress response of tobacco enhances our understanding of oxidative stress regulation under different stress conditions, thereby facilitating tobacco breeding and crop improvement. Similay, pepper (*Capsicum* spp.) is cultivated globally due to its diverse use applications in both food (as a vegetable, spice) and non-food sectors (including industrial and pharmaceutical uses)[38]. However, pepper cultivation faces significant challenges from bacterial diseases such as bacterial wilt,

bacterial spot, and bacterial canker, which threaten global production. Understanding the mechanisms of stress response in peppers can contribute to improving their resistance to stress and enhancing overall yield.

The species diversity in this study allows Machine learning-powered NIR-II fluorescent nanosensors to more comprehensively analyze stress-induced cross-species responses, providing insights into H_2O_2 generation and its role in the stress response of different plant species, revealing commonalities and specificities. The species selection criteria and their relevance to plant stress response studies have now been explicitly discussed in the revised supplemental information (Supplementary Note 18: Applicability of the nanosensor in various plant species).

[Reviewer 1 comment 5] Page 9, Lines 70-77: The interaction mechanism between H_2O_2 and POMs is briefly mentioned. However, a more detailed explanation of how H_2O_2 oxidizes Mo^{5+} to Mo^{6+} and how this leads to changes in NIR absorbance would provide greater clarity. Additionally, the role of oxygen vacancies in enhancing the selectivity toward H_2O_2 should be further elaborated.

[Author Response]: We would like to thank the reviewer for the valuable comments on the sensing mechanism of our nanosensors. The interaction mechanism between H_2O_2 and POMs is critical to the sensing performance, and we recognize the necessity for a more comprehensive explanation.

In POMs, Mo exists in a mixed-valence state (Mo^{5+}/Mo^{6+}). The strong NIR absorption band of POMs is attributed to the localized surface plasmon resonance (LSPR) effect resulting from the charge-transfer transition between Mo^{5+} and Mo^{6+} via oxygen vacancies (Fig. 1b) (*Adv. Funct. Mater.* 33, 2301683 (2023))[10]. H_2O_2 acts as an oxidant agent, converting Mo^{5+} in POMs to Mo^{6+}. This oxidation process reduces the proportion of Mo^{5+}, thereby weakening the intervalence charge transfer (IVCT) effect between Mo^{5+} and Mo^{6+} (*Angew. Chem. Int. Ed.* 62, e202303989 (2023))[39]. Since IVCT is directly related to the NIR absorbance, the oxidation of Mo^{5+} to Mo^{6+} leads to a decrease in NIR absorbance. Supplementary Fig. 8 shows that increasing the concentration of H_2O_2 leads to a gradual reduction in the NIR absorption of POMs.

The presence of oxygen vacancies generates localized defect states on the surface of POMs, which serve as active sites for the adsorption and activation of H_2O_2. These vacancies enhance the interaction between the sensor and the target molecule, thereby accelerating the electron transfer process and improving sensing performance (*Nat. Rev. Chem.* 2, 0112 (2018)[40], *Chem. Rev.* 118, 2680-2717 (2017)[41], *Adv. Funct. Mater.* 33, 2301683 (2023)[10]).

We have included a more detailed description in the revised main text. The revised content is as follows:

"According to the XPS peak area of Mo 3d, the average oxidation states of Mo in Mo-POM, Mo/Fe-POM, and Mo/Cu-POM were determined to be 5.38. 5.49, and 5.40, respectively (Supplementary Table 1), indicating a mixed-valence state resulting from the presence of oxygen vacancies[42]. The strong NIR absorption band of POMs was attributed to the localized surface plasmon resonance (LSPR) effect associated with the charge-transfer transition between Mo^{5+} and Mo^{6+} via oxygen vacancies[43]. Upon reaction with varying concentrations of H_2O_2, Mo^{5+} in the POMs was oxidized to Mo^{6+}, leading to a decrease in the intervalence charge transfer (IVCT) between the mixed-valence Mo centers[39], which is directly correlated with the reduction in the NIR absorbance (Fig. 1b). Oxygen vacancies introduce localized defect states that facilitate the adsorption and activation of H_2O_2 molecules on the surface of POMs and promote more efficient electron transfer[10,40,41], thus expanding the redox tracnsformation from Mo^{5+} to Mo^{6+}." (Page 6-7, line 111-121 in revised manuscript)

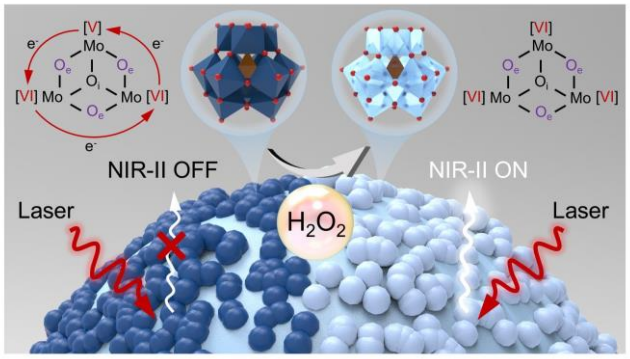

Fig. 1b. Schematic illustrating the responsive mechanism of the nanosensors toward H_2O_2.

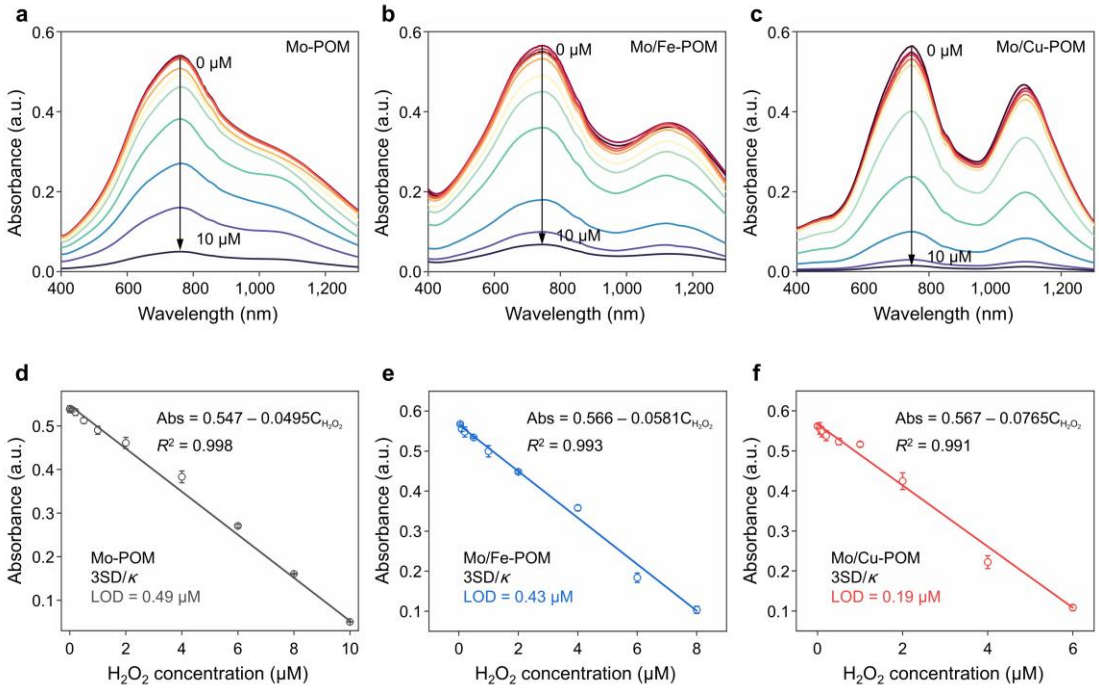

Supplementary Fig. 8. Three POMs respond to H_2O_2. Changes in absorption spectra (a, b, c) and absorbance values (d, e, f) were observed before and after the POMs were exposed to different concentrations of H_2O_2. Data are presented as mean ± s.d. from three independent measurements. The detection limits of Mo-POM, Mo/Fe-POM, and Mo/Cu-POM for H_2O_2 were calculated using the formula 3SD/κ, where SD is the standard deviation of the blank solution and κ is the slope of the calibration curve.

[Reviewer 1 comment 6] Page 9, Lines 79-85: Its advantages over other NIR-II fluorophores in terms of fluorescence efficiency and stability should be quantitatively compared. For example, how does its photostability or quantum yield compare to previously reported NIR-II fluorophores?

[Author Response]: We would like to thank the reviewer for this constructive comment. We have added QY measurements of AIE molecules as well as AIE nanoparticles, to the revised supporting information. Using IR-26 as a reference, the QYs in the NIR-II region for AIE_{1035} and AIE_{1035}NPs in THF and H_2O were determined to be 0.94% and 4.84%, respectively, which are higher than the widely used 0.4% for carbon nanotubes (*Nano Lett.* 7, 3698-3703 (2007))[44] and 0.3% for CH1055-PEG (*Nat. Mater.* 15, 235-242 (2015))[45] (Supplementary Fig. 1d).

Regarding photostability, we measured the fluorescence intensity of AIE_{1035}NPs and that of the commonly used NIR-II molecule, ICG, under continuous laser irradiation at 808 nm (100 mW) for 1 hour (Fig. 2h). The results indicated that, in contrast to the rapid decay of the fluorescence intensity observed in ICG, AIE_{1035}NPs maintained their initial fluorescence intensity and demonstrated good resistance to photobleaching. This excellent photostability is primarily attributed to the robust molecular framework of AIE_{1035}.

These results indicate that our NIR-II fluorescent molecule has significant advantages in terms of fluorescence efficiency and stability, making it a promising candidate for plant NIR-II fluorescence imaging. We have added the relevant analysis in the revised supporting information (Supplementary Note 1: Validation of the AIE effect and quantum yield measurement, and Supplementary Fig. 1d).

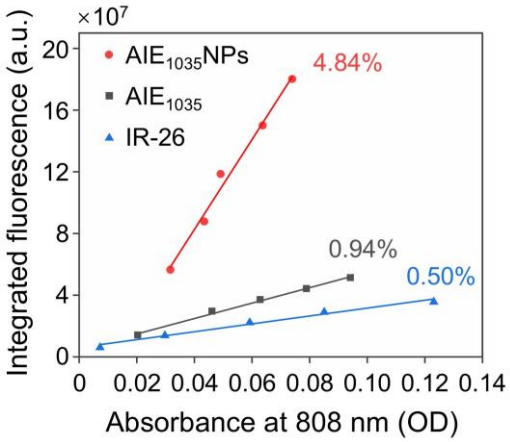

Supplementary Fig. 1d. The plots for the integrated fluorescence intensities of AIE_{1035} in THF, AIE_{1035}NPs in H_2O, and IR-26 in the 1,2-dichloroethane at five different concentrations.

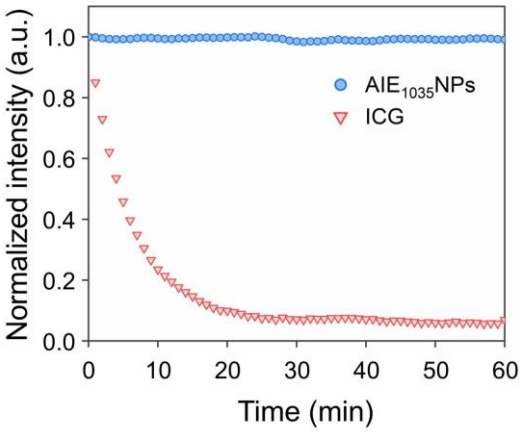

Fig. 2h. Photostability evaluation of the AIE_{1035}NPs dispersion and ICG solutions under constant laser beam exposure for 60 min. Laser excitation: 808 nm, 100 mW.

[Reviewer 1 comment 7] Page 10, Lines 102-110: The characterization results (e.g., TEM, XPS, zeta potential) provide evidence of successful synthesis. However, it would be helpful to compare the dispersion quality and stability of the nanosensors with and without Mo/Cu-POM assembly. Does the presence of Mo/Cu-POM influence the physical stability or aggregation behavior of the nanoparticles?

[Author Response]: We thank the reviewer for this helpful recommendation. Comparing the stability of the nanosensors before and after the assembly of Mo/Cu-POM is valuable for long-term sensing in plants. To address this issue, we conducted an additional three weeks of dynamic light scattering (DLS) measurements to evaluate the colloidal stability of the nanoparticles both with and without the Mo/Cu-POM assembly. The results indicated that the assembly of Mo/Cu-POM did not significantly affect the stability of the sensor, and no aggregation occurred over a long period of time. The revised content is as follows:

" The results of dynamic light scattering (DLS) measurements lasting for three weeks indicated that the assembly of Mo/Cu-POM did not significantly affect the hydrodynamic diameter and PDI of the nanoparticles (Supplementary Fig. 16), thereby demonstrating the long-term stability of the nanosensor." (Page 8, line 144-147 in revised manuscript)

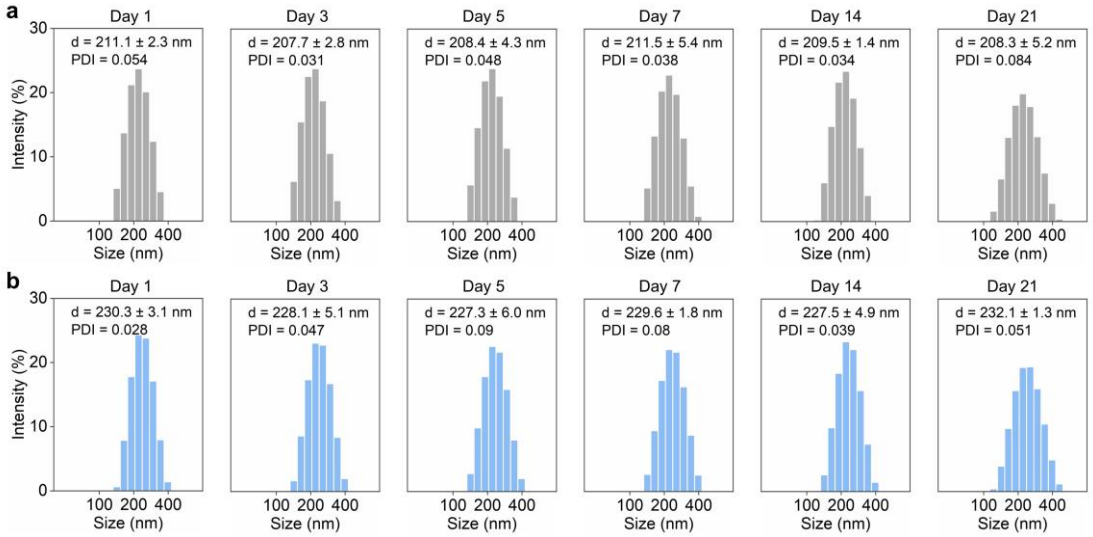

Supplementary Fig. 16. Long-term stability evaluation of the nanoparticles. Size distribution and particle distribution index of the synthesized AIE_{1035}NPs (a) and AIE_{1035}NPs@Mo/Cu-POM (b) in three weeks. Dynamic light scattering (DLS) measurements were conducted to compare the colloidal stability of the nanosensor with and without the Mo/Cu-POM assembly. The particle distribution index (PDI) is a crucial index for evaluating the dispersion performance of nanoparticles. The PDI for DLS typically reflects the intensity of light scattered by various fractions of the particles that differ in sizes and is calculated using the formula $(width/mean)^2$ for each peak. A PDI of ≤ 0.1 is considered to be highly monodisperse, while value between 0.1 to 0.4 is regarded as moderately polydisperse, and value greater than 0.4 is classified as highly polydisperse[46].

[Reviewer 1 comment 8] Page 12, Lines 127-140: It would be helpful to quantify this relationship. For instance, it is suggested to provide data or metrics that compare the degree of spectral overlap to the resulting quenching efficiency for each AIE luminophore.

[Author Response]: We thank the reviewer for the constructive comments. In this study, we used a broad-absorption fluorescent quencher (Mo/Cu-POM) in conjunction with five AIENPs, whose absorption and emission spectra span the range from visible light to near-infrared. To investigate the relationship between the degree of spectral overlap and the modulation of fluorescence emission, we calculated the integral overlap between the absorption and emission spectra of each AIENP and the characteristic absorption peak of the quencher. Additionally, we measured the corresponding fluorescence quenching constant (*K*). The results indicated that AIENPs with a greater degree of spectral overlap exhibit higher quenching efficiency (AIE_{955} and AIE_{1035}), while nanoparticles with less spectral overlap have lower quenching efficiency (AIE_{475}, AIE_{520}, and AIE_{712}).

We have added a spectral overlap analysis for each AIENPs in relation to the quencher, as well as the calculation of the fluorescence quenching constant, in the revised manuscript and supporting information (Supplementary Fig. 20-21 and Supplementary Note 7: Modulation of five AIE fluorescence by Mo/Cu-POM). The relevant changes

in the revised manuscript are as follows:

"To investigate the imaging performance of fluorescent molecules with different emission bands in plants, we co-assembled five AIE luminophores with varying excitation and emission wavelengths with Mo/Cu-POM (Fig. 2a-c). There was insufficient overlap between the absorption spectrum of Mo/Cu-POM and the ultraviolet-visible absorption and fluorescence emission spectra of AIE_{475} and AIE_{520} with a tetrastyrene structure (Supplementary Fig. 20). In contrast, the spectra of AIE_{712} showed partial overlap with the characteristic absorption peak of Mo/Cu-POM. Notably, the spectra of the NIR-II fluorescent AIE_{955} and AIE_{1035} nearly coincided with the broad absorption peak of Mo/Cu-POM. Due to these varying degrees of spectral overlap, the extent of fluorescence quenching differed significantly among the AIENPs (Fig. 2d). We employed the spectral overlap integral and the fluorescence quenching constant (K) to evaluate the ability of Mo/Cu-POM to modulate the fluorescence emission of the nanoparticles (Supplementary Fig. 20, 21). The results revealed that both the spectral overlap integral and the quenching constant of Mo/Cu-POM were greater for NIR-II FL nanoparticles compared to those that are visible and NIR-I fluorescent. These findings suggest that the fluorescence quenching effect of Mo/Cu-POM on AIENPs is critically determined by the spectral overlap and can be further optimized by adjusting the concentration of Mo/Cu-POM." (Page 8-9, line 157-172 in revised manuscript)

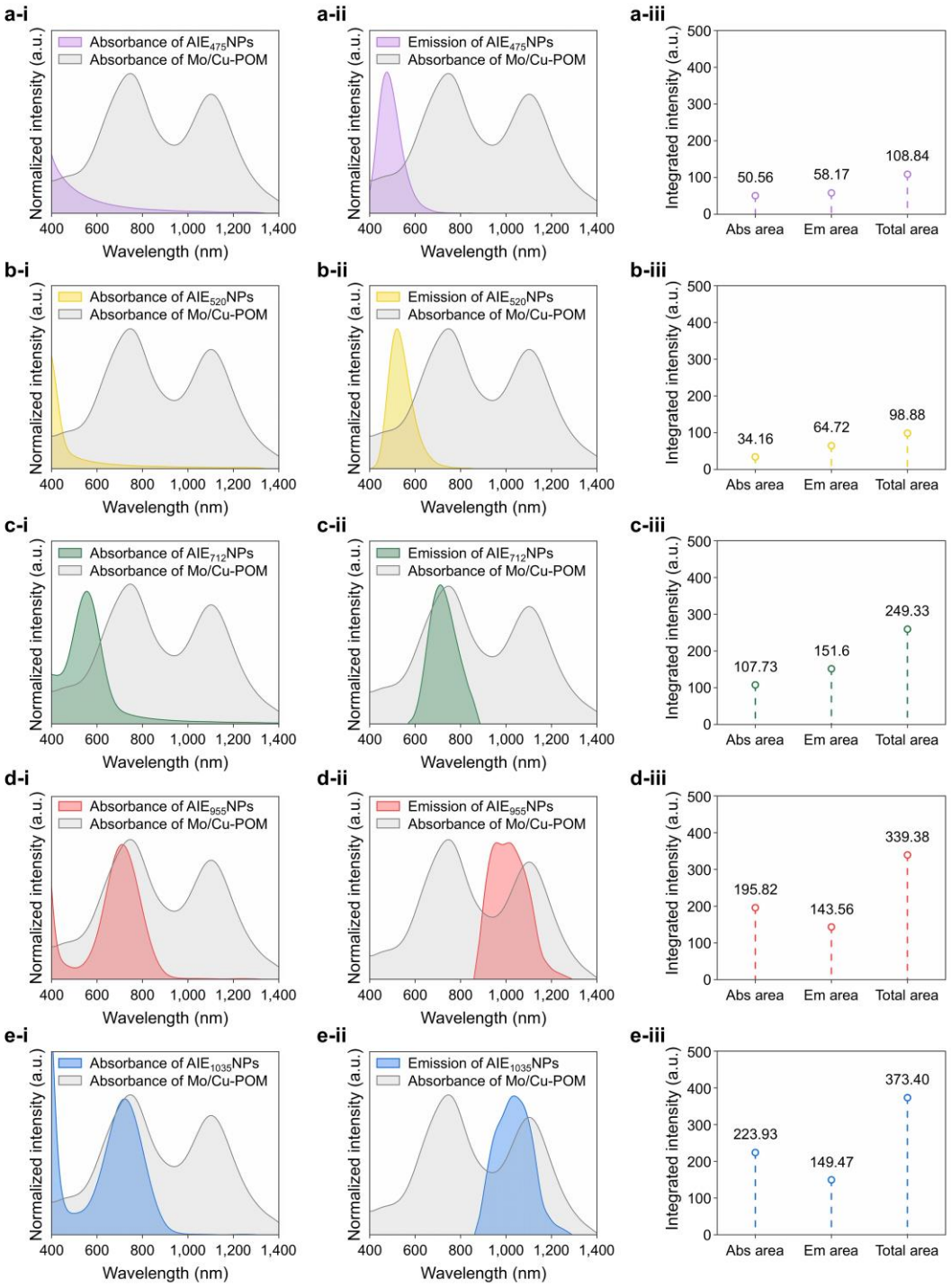

Supplementary Fig. 20. The degree of spectral overlap between the quencher and the AIE nanoparticles. (i) Overlap of the Mo/Cu-POM absorbance spectrum with the absorbance spectra of AIENPs. (ii) Overlap of the Mo/Cu-POM absorbance spectrum with the fluorescence emission spectra of AIENPs. (iii) Integration of spectral overlap between the quencher and AIE nanoparticles.

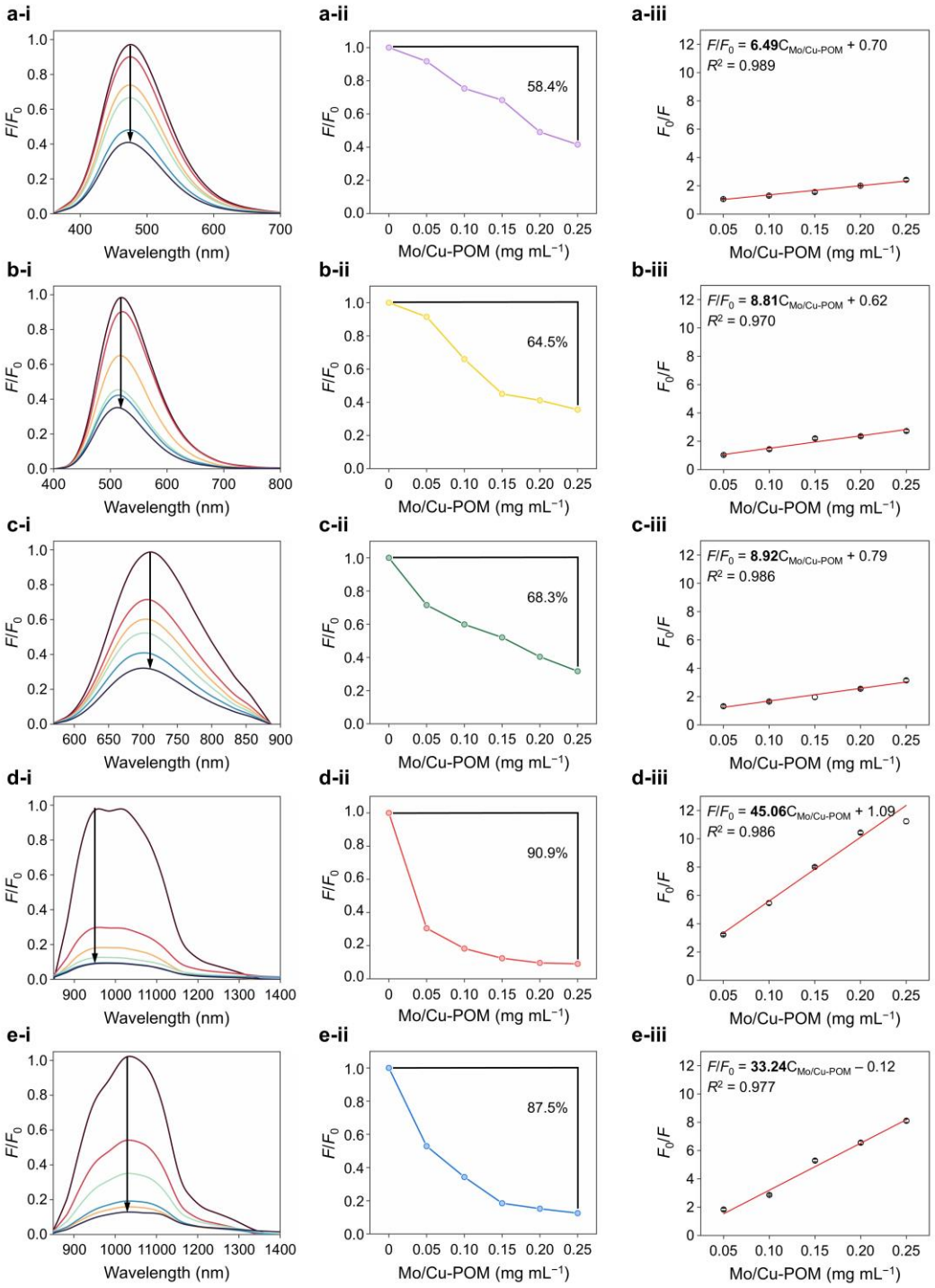

Supplementary Fig. 21. Potential of Mo/Cu-POM to modulate the fluorescence emissions of five AIENPs. (i) Emission spectra of AIE_{475}NPs@Mo/Cu-POM (a), AIE_{520}NPs@Mo/Cu-POM (b), AIE_{712}NPs@Mo/Cu-POM (c), and AIE_{955}NPs@Mo/Cu-POM (d), and AIE_{1035}NPs@Mo/Cu-POM (e) at varying concentrations of Mo/Cu-POM (0-0.25 mg mL^{-1}) , arranged top to bottom. (ii) Plot illustrating the changes in fluorescence intensity ratios as a function of Mo/Cu-POM concentration. The fluorescence quenching efficiencies of 0.25 mg mL^{-1} Mo/Cu-POM

for the five AIENPs were 58.4% (AIE_{475}), 64.5% (AIE_{520}), 68.3% (AIE_{712}), 90.9% (AIE_{955}), and 87.5% (AIE_{1035}). F_0 and F denote the emission peak values of the AIENPs before and after their assembly with Mo/Cu-POM, respectively. (iii) Stern–Volmer calibration curves of Mo/Cu-POM.

[Reviewer 1 comment 9] Page 14, Lines 179-184: The lack of significant changes in FV/FM and the propidium iodide assay results strongly support the nanosensor's biocompatibility. It is suggested to briefly discuss whether these observations hold across different environmental conditions (e.g., drought stress or varying light intensities).

[Author Response]: We thank the reviewer for the suggestion. We agree that it is necessary to demonstrate the applicability of this result under different cultural conditions. In supplementary tests, the health status of pepper plants was evaluated using F_V/F_M and PI assays across various treatment conditions. Soil moisture levels were manipulated to represent distinct stages following irrigation: the day of watering (~35% soil moisture), three days post-watering (~20% soil moisture), and ten days post-watering (<5% soil moisture). Light conditions were regulated by placing the plants in an artificial climate chamber with varying light intensities ranging from 100 to 200 $\mu mol\ m^{-2}\ s^{-1}$. We found that the nanosensor maintained its inherent biocompatibility under a range of environmental conditions, including drought stress and varying light intensities. The relevant changes in the revised manuscript and supporting information (Supplementary Fig. 30, 32, and Supplementary Note 12: Biocompatibility of the nanosensor in plants) are as follows:

"Considering that various environmental factors, such as soil moisture and light conditions, can influence plant physiology, the compatibility of the nanosensor under different stress conditions was further evaluated (Supplementary Fig. 30, 32)." (Page 11, line 216-218 in revised manuscript)

Supplementary Note 12: Biocompatibility of the nanosensor in plants

In extreme environments where soil moisture is less than 5% (measured on the 10th day after watering), the pepper leaves showed signs of physiological stress (Supplementary Fig. 30, 32). The group treated with the nanosensors under the same

culture conditions did not show significant differences, indicating the biocompatibility of the nanosensor under various growth conditions.

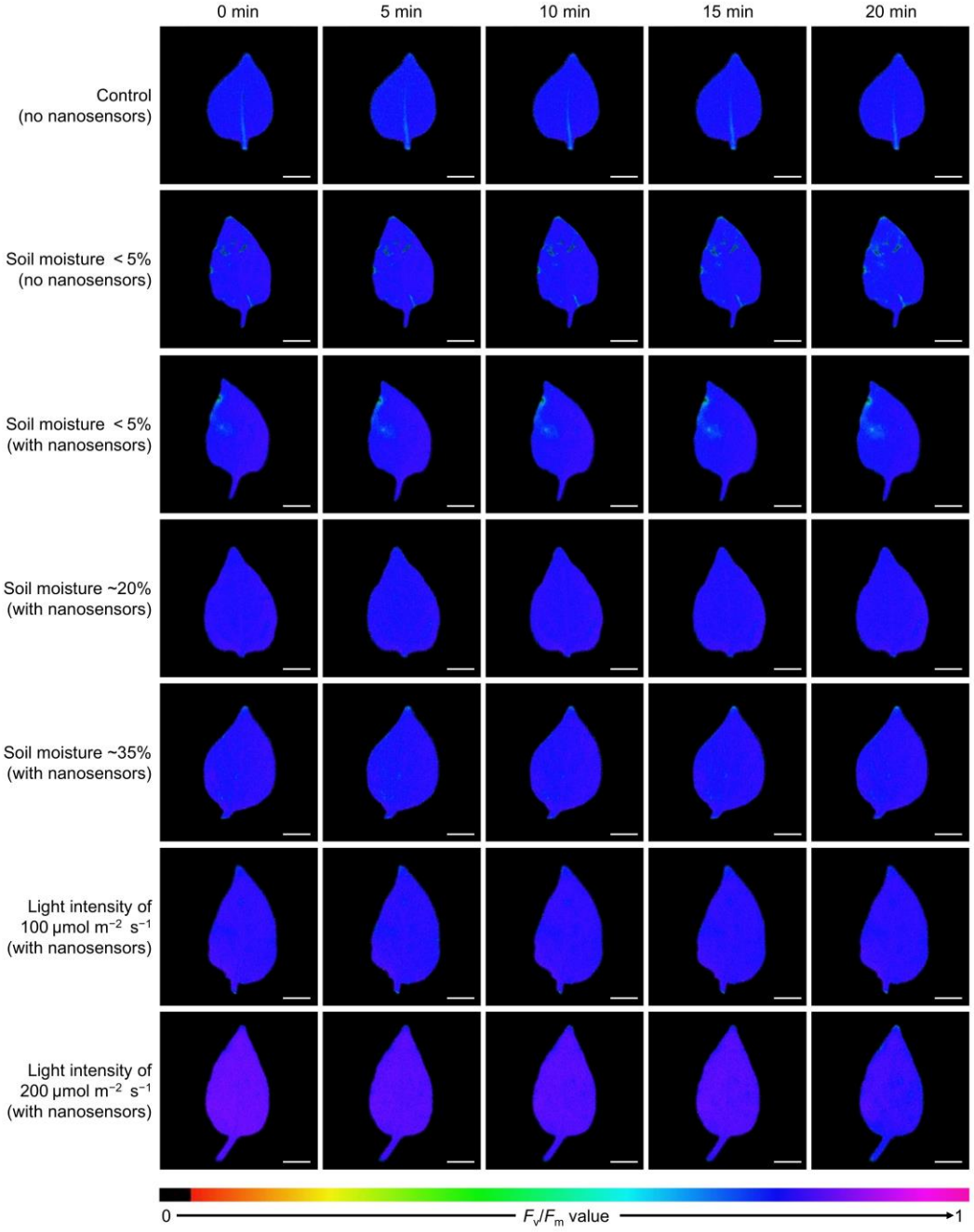

Supplementary Fig. 30. Chlorophyll fluorescence image of pepper leaves treated with nanomaterials under various cultivation conditions. Two-month-old pepper plants were grown under different conditions, after which the leaves were injected with nansensors. Scale bar: 1 cm.

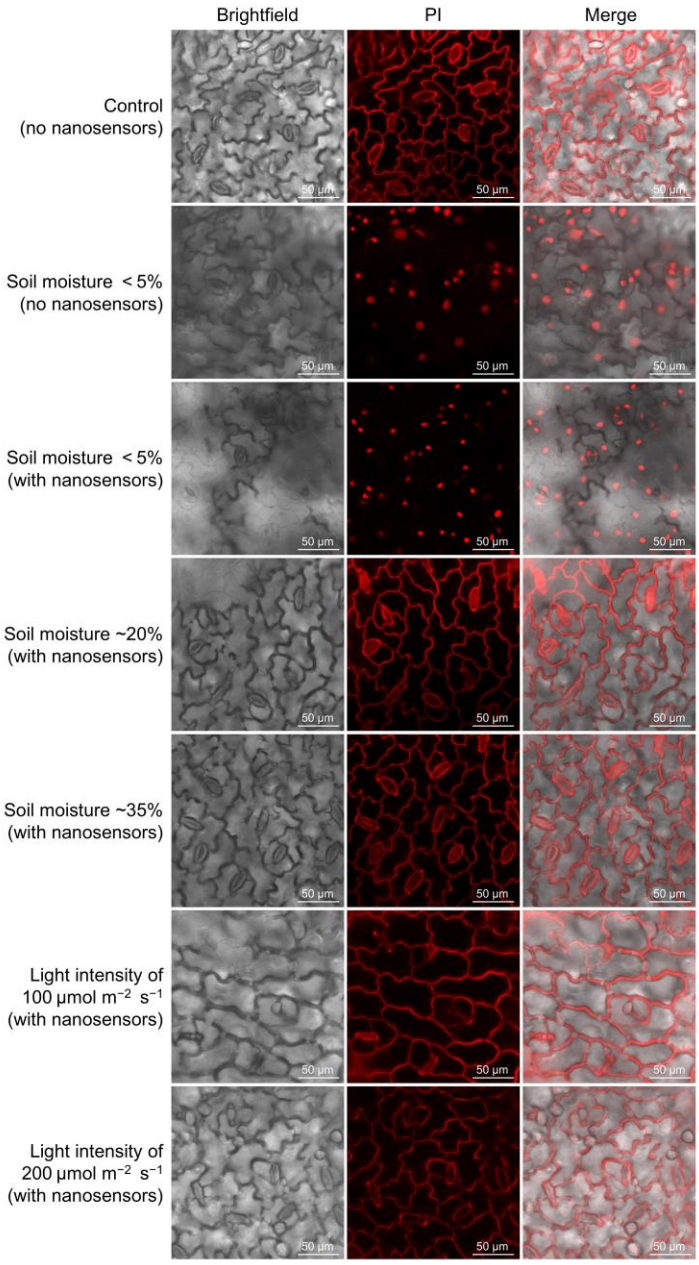

Supplementary Fig. 32. Confocal fluorescence micrographs of propidium iodide-stained pepper leaves under different culture conditions.

[Reviewer 1 comment 10] Page 15, Lines 187-197: Particularly in terms of detection limits and dynamic range, how does the designed nanosensor's sensitivity compare to other reported H_2O_2 sensors.

[Author Response]: Thank you for the valuable comment. We have provided a detailed comparison of our nanosensor's detection limit, dynamic range, and other performance parameters with those of other reported H_2O_2 sensors in Supplementary Table 2. The detection limit of our nanosensor (0.43 µM) is significantly lower than that of other

reported H_2O_2 sensors, such as 2.76 μM in *Chem. Eng. J.* 464, 142496 (2023)[5], 10 μM in *Nano Lett.* 21, 2625-2633 (2021)[9], and 16.2 μM in *Angew. Chem. Int. Ed.* 60, 15809-15815 (2021)[8]. The dynamic range of our sensor (1-40 μM) also surpasses that of several other reported H_2O_2 sensors, including 0-10 μM in *Nat. Commun.* 12, 6870 (2021)[7] and 0.5-3 μM in *Adv. Funct. Mater.* 33, 2301683 (2023)[10]. The revised content is as follows:

"The sensor's sensitivity of 0.43 μM and response time of 1 min surpass those of existing NIR-II sensors, enabling rapid, real-time monitoring of trace levels of H_2O_2."

(Page 4-5, line 72-74 in revised manuscript)

[Reviewer 1 comment 11] Consider that expanding on the practical implications of achieving a classification accuracy of 96.67%. It could provide a more balanced view by including comments, for example, how might this accuracy translate to real-world applications in agriculture or environmental monitoring? discussing any challenges or limitations encountered during ML implementation.

[Author Response]: We thank the reviewer for this meaningful suggestion. In recent years, the significant advantages of ML in data analysis and noise reduction have led to numerous attempts to integrate it with sensors for plant disease detection, stress phenotype analysis, and predictive analytics, including plant wearable sensors (*Sci. Adv.* 9, eade2232 (2023)[47]; *Sci. Adv.* 10, eadk7488 (2024)[48]), electrochemical sensors (*Sci. Adv.*10, eadj6315 (2024)[49]; *Biosens. Bioelectron.* 271, 117062 (2025)[50]) and acoustic sensor (*Cell* 186, 1328–1336 (2023)[51]). However, ML models have not yet been developed for in-situ stress detection and stress analysis of NIR-II fluorescence imaging systems. In this work, we have outlined the significant advantages of NIR-II fluorescent nanosensors for monitoring plant stress, including their non-destructive nature, real-time capabilities, and ability to circumvent the inherent fluorescence background of plants. The application of this technology to analyze stress signals across various species and environments is crucial for understanding the physiological response mechanisms of plants. Given that plant stress monitoring is a continuous process, hundreds of fluorescence images may be generated for each sample throughout the

experiment. When multiple species and stresses are monitored dynamically, the amount of data can escalate to tens of thousands of images, which is clearly unmanageable manually. This study is the first attempt to integrate NIR-II fluorescence plant sensors with ML, yielding promising preliminary results in sensing performance and stress identification.

Some challenges and limitations must be addressed to improve the applicability of ML in NIR-II fluorescence imaging signal analysis. Although the XGBoost-based ML analysis framework demonstrated high accuracy in stress classification, its training was confined to the specific plant species selected for this work, including lettuce, spinach, tobacco, and pepper. Future work should prioritize expanding the training dataset, facilitating the monitoring of sensors under various stress conditions, and ensuring applicability to a broader range of species. Additionally, considerations regarding cost and portability are essential for field applications. We have added the challenges encountered during the implementation of ML and outlined the direction for future research in the discussion section. The revised content is as follows:

"Considering that the NIR-II fluorescent nanosensor combined with ML model enables rapid and accurate identification of plant stress, it presents new opportunities for agricultural and environmental monitoring. ML-based automated analysis methods can rapidly swiftly signals, analyze trends, and classify stress from large volumes of continuously captured images (tens of thousands), which far exceeds the capabilities of manual processing. Plants embedded with nanosensors serve as sentinels, facilitating the early, asymptomatic detection of biotic and abiotic stressors within a short timeframe (a few hours), thereby promoting targeted pest and disease management, as well as early stress response strategies to minimize crop losses. Furthermore, integrating nanosensor technology with environmental monitoring systems may facilitate the assessment of ecosystem health and the early detection of environmental degradation. For practical field applications, it is advisable to utilize portable and cost-effective electronic devices, such as Raspberry Pi, connected to small infrared cameras for imaging. However, ML models trained on datasets obtained under laboratory conditions may not be directly applicable to fluorescence signals collected by portable

imaging devices, which typically exhibit lower sensitivity. Therefore, it is essential to train separate models on datasets sampled outdoor to enhance accuracy. Updated ML models must incorporate robust noise-filtering techniques to effectively distinguish stress signals from environmental noise. The relatively small number of experiments in the dataset for this study limits the scalability of the ML models and increases the potential for distortion due to outliers. Future research should focus on expanding the training dataset, extending sensor monitoring to encompass various stress conditions, and improving its applicability across a broader range of plant species." (Page 20-21, line 402-422 in revised manuscript)

Reviewer #2 (Remarks to the Author)

I co-reviewed this manuscript with one of the reviewers who provided the listed reports. This is part of the Nature Communications initiative to facilitate training in peer review and to provide appropriate recognition for Early Career Researchers who co-review manuscripts.

[Author Response]: Thank you for reviewing our manuscript. We sincerely appreciate the effort you and your co-reviewer have put into the review process. We highly value all the insightful comments provided by the reviewers, which have helped us improve the manuscript. Please refer to the revised document for our detailed responses to each issue.

Reviewer #3 (Remarks to the Author)

The manuscript presents an innovative approach by integrating machine-learning-powered NIR-II fluorescent nanosensors for real-time, non-invasive monitoring of plant stress responses, specifically focusing on H_2O_2 signaling. The study showcases a strong experimental foundation and demonstrates the application of the technology across multiple plant species. However, some areas require further elaboration and clarification. Below is a detailed review:

The strengths of this work are evident. The integration of a fluorescence "turn-on" mechanism with machine learning to classify stress types is a major contribution to the field of agricultural diagnostics. The nanosensor's ability to bypass background autofluorescence and provide real-time, species-independent stress monitoring addresses key limitations in current plant sensing technologies. Furthermore, the study demonstrates impressive validation across various plant species, solidifying the robustness and universality of the approach. The use of machine learning, particularly XGBoost, for stress classification and its high accuracy of up to 96.67% for identifying specific stressors adds a layer of scalability and applicability to the technology. Despite these strengths, the manuscript has some weaknesses and areas for improvement.

[Author Response]: We sincerely appreciate your thorough review and constructive comments on our manuscript. We have made substantial revisions and incorporated additional experimental data to address the concerns raised. We believe these modifications have significantly enhanced the clarity and robustness of our study. Below, we address each comment point by point, and the specific changes made to the manuscript in response to each point are highlighted in ***yellow***.

[Reviewer 3 comment 1] The introduction could better contextualize the limitations of existing technologies by offering a detailed comparison of their shortcomings.

[Author Response]: We thank the reviewer for this meaningful suggestion. Current methods used for monitoring plant stress responses mainly include histochemical staining, genetically encoded fluorescent probes, and wearable plant sensors.

Histochemical staining necessitates the destruction of samples and does not allow for real-time monitoring. Genetically encoded fluorescent probes enable non-destructive detection, however, they are primarily limited to model plants (e.g., *Arabidopsis thaliana*) and require complex genetic modifications, which pose challenges for large-scale agricultural applications. Wearable plant sensors mainly focus on physiological information from the plant's surface, such as humidity, leaf temperature, and volatile gases, with limited studies on intracellular signaling molecules. Our machine learning-based NIR-II activatable fluorescent nanosensor addresses these limitations, enabling high-sensitivity, non-destructive, species-independent, and real-time monitoring of stress signals in plants. We have thoroughly compared the limitations of the previous methods in the introduction to emphasize the advantages of the nanosensors presented in this study for monitoring of plant stress. The revised content is as follows:

"Detecting stress-induced signals in living plants presents significant challenges due to their low concentrations and the frequent coexistence of various other active substances[52-55]. Current methods for sensing stress-induced signals primarily rely on histochemical reagents following the isolating and purification of plant extracts[56-58]. However, these methods are typically destructive and do not permit real-time tracking of the endogenous dynamic signals. Furthermore, genetically encoded molecular sensors for stress signaling, as a non-destructive approach, predominantly focus on the stress-specific signal transduction pathways triggered in the model plant *Arabidopsis thaliana*, making them time-consuming for phenotypic expression and screening[23,25,59,60]. Given that most crops are non-model plants, studying the stress signaling patterns of these crops places greater demands on the existing detection techniques. Nanotechnology-based sensors are species-independent and can detect stress responses in various wild-type plants by monitoring plant health in real-time through electronic devices, eliminating the need for genetic engineering[4,47,61-66]. The latest plant advancements in wearable sensors and electrochemical sensors enable non-destructive and continuous acquisition of phenotypic data. Wearable electronic devices monitor plant conditions by capturing physical signals such as growth, surface temperature, and humidity[48,67], as well as chemical signals like volatile organic

compounds[47], and bioelectrical potential signals[68]. From flexible sensors wrapped around the stem to the epidermal electronics that can be seamlessly attached to leaves, most efforts have focused on acquiring physiological information from the plant's surface. Direct detection of trace molecules in the cytosol and intercellular spaces can provide deeper insights into the signaling network involved in plant stress responses. In contrast to lagging physiological indicators (such as strain, moisture, or leaf temperature), stress-induced real-time signaling molecules (including reactive oxygen species, phytohormones, and inorganic ions) reflect early stress responses before the appearance of visible stress symptoms." (Page 3-4, line 47-58 in revised manuscript)

[Reviewer 3 comment 2] The manuscript does not address the scalability of this approach for field applications, which is critical for its adoption in agriculture.

[Author Response]: We appreciate the reviewer for raising this critical issue. To meet the demands of smart agriculture, an ideal plant stress monitoring system should be applicable to various plant species, capable of real-time operation, and scalable for large-scale deployment. Our ML-powered NIR-II activated fluorescence nanosensor is species-independent and can be utilized across multiple plant species without the need for genetic modification. This advantage overcomes the limits of transgenic approaches, thereby enhancing the feasibility of large-scale deployment. Furthermore, our ML model significantly enhances data processing efficiency, enabling the high-accuracy automated classification of plant stress responses. This capability facilitates large-scale phenotypic analysis and early stress detection, which are essential for improving crop resilience and yield.

Currently, the datasets of ML model are mainly collected under laboratory and greenhouse conditions. For practical field applications, nanosensors need to be combined with portable imaging systems. Small infrared cameras connected to low-cost, portable electronic devices, such as the Raspberry Pi—a compact, credit card-sized device priced at $35—can enable efficient imaging in field environments. These affordable tools can be used to capture signals during field applications. We have added a discussion on the scalability and challenges of this approach in field applications in

the revised manuscript. The revised content is as follows:

"For practical field applications, it is advisable to utilize portable and cost-effective electronic devices, such as Raspberry Pi, connected to small infrared cameras for imaging. However, ML models trained on datasets obtained under laboratory conditions may not be directly applicable to fluorescence signals collected by portable imaging devices, which typically exhibit lower sensitivity. Therefore, it is essential to train separate models on datasets sampled outdoor to enhance accuracy. Updated ML models must incorporate robust noise-filtering techniques to effectively distinguish stress signals from environmental noise. The relatively small number of experiments in the dataset for this study limits the scalability of the ML models and increases the potential for distortion due to outliers. Future research should focus on expanding the training dataset, extending sensor monitoring to encompass various stress conditions, and improving its applicability across a broader range of plant species." (Page 20-21, line 411-422 in revised manuscript)

[Reviewer 3 comment 3] The potential long-term impacts of introducing nanosensors on plant health and soil ecosystems are not discussed.

[Author Response]: We thank the reviewer for the comprehensive comments. Assessing the potential long-term impact of introducing nanosensors on plant health and soil ecosystems is essential to ensure their safe and sustainable application in agriculture. We have added an evaluation of the long-term effects of nanosensors on plant health in the revised manuscript. During the three-week monitoring period, there were no negative effects of the nanomaterial treatment on the overall growth and chlorophyll content of *Arabidopsis* and pepper (Supplementary Fig. 33).

Since the diffusion of nanosensors in plants is limited, they do not directly enter the soil or affect the soil ecosystem. We speculate that the potential accumulation of nanosensors in plant tissues may indirectly affect the physical and chemical properties of the soil by altering root-secreted compounds. To assess this possibility, we analyzed the physical and chemical properties of the cultivated soil before and after nanosensor treatment. No significant differences were observed in pH, total nitrogen, total

phosphorus, total potassium, organic matter, or microbial biomass carbon between the water-injected control group and the nanosensor-treated group (Supplementary Table 3). In the long-term evaluation, nanosensors showed no adverse effects. We have revised the manuscript to discuss the potential long-term impacts of introducing nanosensors on plant health and soil ecosystems. The revised content is as follows:

"In long-term assessments, nanomaterial treatments did not adversely affect the overall growth and chlorophyll content of *Arabidopsis* and peppers, nor did they impact the physical and chemical properties of the soil (Supplementary Fig. 33 and Supplementary Table 3)." (Page 11, line 218-221 in revised manuscript)

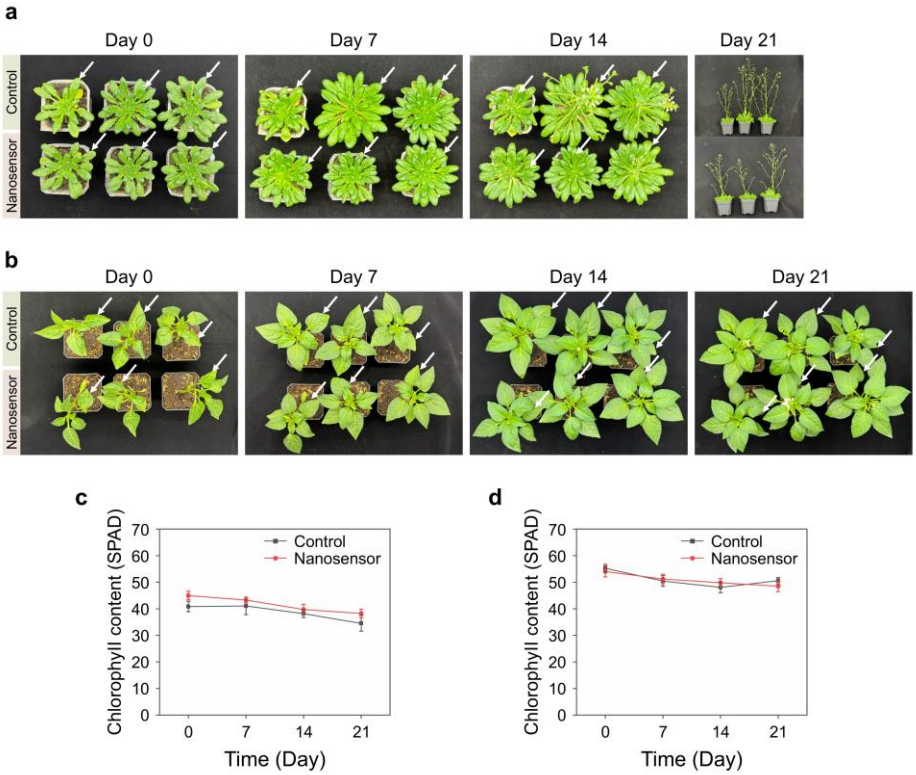

Supplementary Fig. 33. Long-term biocompatibility evaluation of nanosensors. AIE_{1035}NPs@Mo/Cu-POM-infiltrated *Arabidopsis* (a) and pepper (b) plants exhibited no significant differences in overall growth compared to control plants infiltrated with water.

Supplementary Table 3. Assessment of changes in soil ecosystems before and after application of nanosensors to plant leaves.

Sample	pH	Total nitrogen (g kg^{-1})	Total phosphorus (g kg^{-1})	Total potassium (g kg^{-1})	Organic matter (g kg^{-1})	Microbial biomass carbon (mg kg^{-1})
Control Day 0	6.89 ± 0.13	3.92 ± 0.24	0.32 ± 0.01	4.12 ± 0.17	29.62 ± 1.16	196.36 ± 1.82
Control Day 15	6.83 ± 0.14	3.88 ± 0.22	0.36 ± 0.02	4.10 ± 0.19	31.42 ± 0.25	201.52 ± 2.38
Control Day 30	6.78 ± 0.09	4.16 ± 0.23	0.34 ± 0.02	4.10 ± 0.10	28.18 ± 1.49	197.66 ± 4.43
Nanosensors Day 0	6.79 ± 0.06	3.88 ± 0.16	0.31 ± 0.01	4.08 ± 0.19	29.82 ± 0.55	199.35 ± 3.43
Nanosensors Day 15	6.94 ± 0.14	3.60 ± 0.22	0.32 ± 0.01	4.10 ± 0.19	28.75 ± 1.49	196.03 ± 4.62
Nanosensors Day 30	6.87 ± 0.10	3.85 ± 0.19	0.31 ± 0.02	4.07 ± 0.18	28.36 ± 0.55	200.75 ± 2.82

[Reviewer 3 comment 4] The use of machine learning in the study is commendable but lacks depth in explaining how features were extracted and used for stress classification. Furthermore, it is unclear whether the model would generalize well to untrained plant species or stress types. The authors could expand on the interpretability and adaptability of their machine learning mode.

[Author Response]: We thank the reviewer for their insightful comments. The application of ML in our study is crucial for enhancing the accuracy and efficiency of stress classification based on fluorescence signals obtained from the NIR-II nanosensor. To address the reviewer's concerns, we provide a more detailed explanation of feature extraction and the generalizability of our model.

Considering that plant stress monitoring is a continuous process, hundreds of fluorescence images may be generated for each sample during the experiment. When multiple species and stresses are dynamically monitored, the amount of data can reach tens of thousands of images, rendering manual management unfeasible. This study is the first attempt to integrate the NIR-II fluorescence plant sensor with ML. For signal preprocessing and feature extraction, the monitoring and data collection process was completed within 1 hour. Images were continuously acquired using the NIR-II imaging system at a sampling frequency of T = 20 s. The site of probe injection in the plant

served as the fixed location for signal extraction, and the NIR-II signal was collected for 1 h to create the raw time series data. Feature extraction was validated prior to ML analysis by projecting the multidimensional feature space into 2D space using t-distributed stochastic neighbor embedding (t-SNE). To obtain the time series segments, all raw data were averaged in batches and summarized for input into the plant stress identification model. The features of each sample were normalized before entering the machine learning (ML) pipeline to enhance the model's generalizability. After data collection and analysis, the training and testing datasets were shuffled and divided in a 7:3 ratio, respectively. We have included a more detailed description of the classification of features in the revised main text. The revised content is as follows:

"Initially, the multidimensional feature space was projected into a two-dimensional space using the t-distributed stochastic neighbour embedding (t-SNE) visualization method, resulting in a scatter plot of the data features (Fig. 6c and Supplementary Fig. 44). t-SNE maps the high-dimensional data into a low-dimensional space while preserving the local similarities between data points, which can reveal the clustering structure of the data and facilitate the understanding of natural groupings within the dataset[69,70]. The data of unstressed and stressed conditions naturally formed different clusters, demonstrating the discriminative power of the features." (Page 17, line 333-340 in revised manuscript)

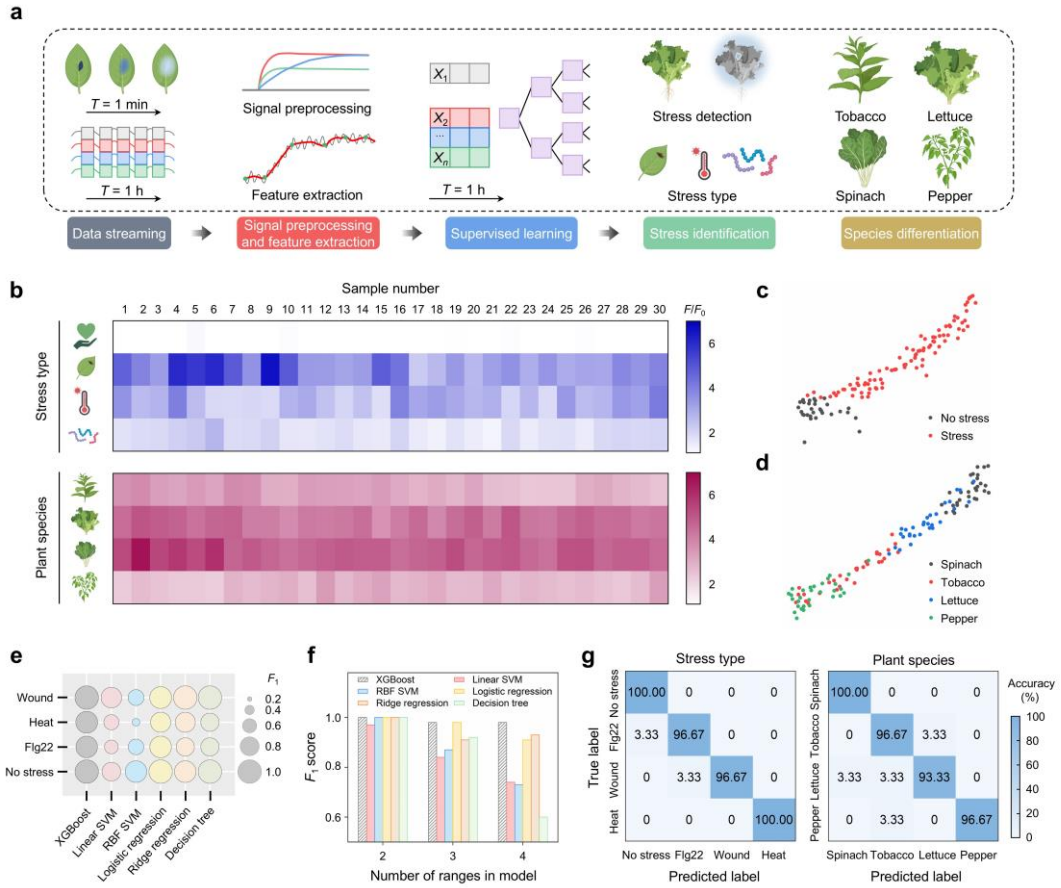

Fig. 6 | ML-powered plant stress status monitoring. a, Schematic of the ML architecture for signal preprocessing, feature extraction, supervised learning, stress identification, and species differentiation. **b,** Heat maps of fluorescence changes in nanosensors monitoring different stress types and plant species over an hour. The intensity levels represent the changes in F/F_0 of nanosensors in lettuce leaves under different stress conditions, including no stress, wound, heat, and flg22 treatment (top panel), as well as in response to mechanical damage across different plant species, including tobacco, lettuce, spinach, and pepper leaves (bottom panel). **c, d,** t-distributed stochastic neighbour embedding plots for the no stress and stress datasets (**c**) and different species stress datasets (**d**). Visual clustering results showed the feature separation in two-dimensional space. **e,** F_1 scores (a metric of accuracy combing precision and recall) of different ML models for stress classification. **f,** F_1 scores of different ML models across an increasing number of ranges categorized by stress identification. The ranges of stress classification include 2 ranges (no stress/stress), 3 ranges (no stress/biotic stress/abiotic stress), and 4 ranges (no stress/flg22/wound/heat). **g,** Confusion matrices of an XGBoost model displaying the classification accuracy for predicting each type of stress and different plant species.

Regarding model generalizability, we conducted additional experiments to assess whether the trained model could effectively classify stress responses across various plant species. Our nanosensor was designed to be species-independent, and we demonstrated that its ability to capture variations in H_2O_2 signals among different plants, including lettuce, spinach, pepper, and tobacco (Fig. 6b). To evaluate the adaptability of the ML model, we tested its performance on stress data from a range of plant species. The results indicate that the classifier maintained high accuracy (Fig. 6g), suggesting that the model generalizes well to other plants exhibiting similar physiological responses. However, we acknowledge that further training with a more diverse dataset would further improve its predictive capability, which we plan to explore in future studies. The identification of stress across a wide range of plant species in the revised manuscript is as follows:

"Additionally, mechanical damage treatment was applied to different plants, including tobacco, lettuce, spinach, and pepper. The site of probe injection in each plant served as a fixed location for signal extraction, and the NIR-II signal was continuously recorded and automatically extracted for one hour to generate the raw time series data. All signals were calibrated and normalized to ensure that the features extracted after data preprocessing were applicable to the overall dataset (Fig. 6a)." (Page 15, line 295-300 in revised manuscript)

"We also collected a dataset of fluorescence signals from different plant species, ies, including tobacco, lettuce, spinach, and pepper, subjected to mechanical damage, which was used for machine learning to differentiate H_2O_2 signal waves across the various species. The XGBoost ML model achieved over 93.33% recognition accuracy among these plant species (Fig. 6g)." (Page 18, line 354-358 in revised manuscript)

[Reviewer 3 comment 5] While the study mentions diffusion limitations of nanosensors within plant tissues, it does not propose solutions or alternative delivery methods to overcome this challenge.

[Author Response]: We appreciate the feedback from the reviewer. Although the diffusion limitations of nanosensors within plant tissues may seem like a constraint,

they also present an opportunity for localized monitoring of stress signals. By confining the nanosensor to specific regions, we can achieve targeted detection of stress-induced signaling molecules, alleviating concerns about uncontrolled diffusion throughout the leaf tissue. This approach enhances the spatial precision of stress detection, allowing for a more accurate interpretation of localized plant responses.

Our group has developed supplementary sensing strategies to overcome diffusion constraints and extend detection capabilities to other plant structures. For instance, we have designed microneedle patches for application on plant stems, enabling direct monitoring of stress-related biochemical changes at the vascular level (Reviewer-only Fig. 5). Additionally, we have employed nanosensors capable of root uptake from hydroponic and soil environments to monitor stress responses in the rhizosphere (Reviewer-only Fig. 6). These alternative delivery methods facilitate comprehensive stress sensing across different plant organs, offering a more holistic understanding of plant stress physiology. We have discussed additional sensing methods in the revised manuscript. The revised content is as follows:

"In addition to blade-based sensing, microneedle patches designed for stem applications provide direct access to vascular signals[71,72], while nanosensors capable of root uptake facilitate stress detection in both hydroponic and soil environments[18,19]. These complementary approaches broaden the scope of plant stress sensing beyond leaf tissues, offering an integrated perspective on stress responses across different plant organs (Supplementary Table 4)." (Page 19-20, line 396-401 in revised manuscript)

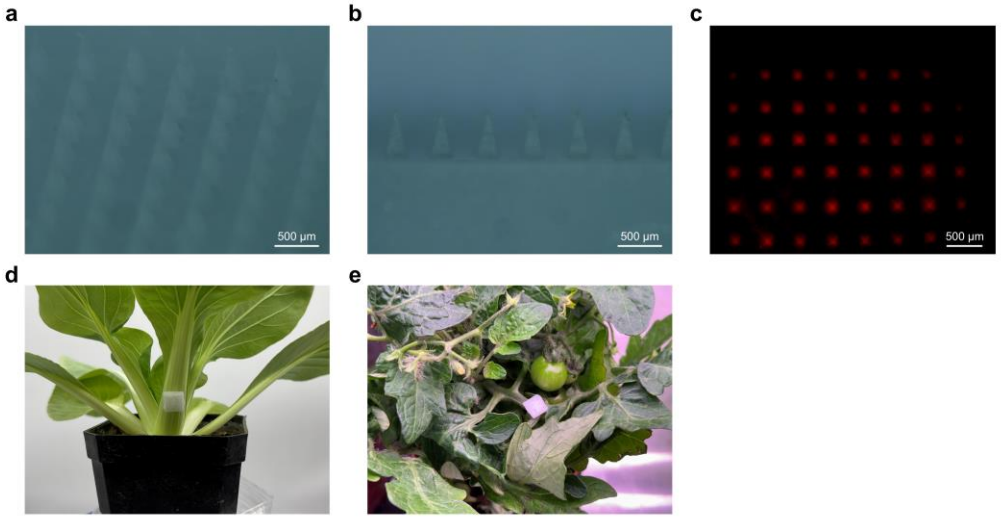

Reviewer-only Fig. 5 | Microneedle patches for detecting stress signals in plant vasculature. (a), (b) Microscope images of the microneedle patch. (c) NIR-II image of the microneedle patch at an excitation wavelength of 808 nm. Photos of the pak choi (d) and tomato plants (e) with microneedle patches applied.

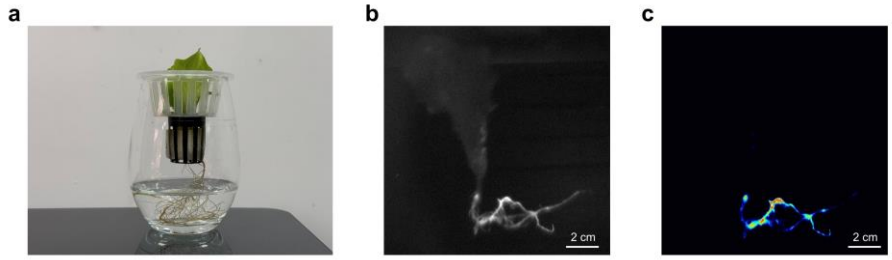

Reviewer-only Fig. 6 | NIR-II fluorescent nanosensors for detecting stress signals in plant roots. (a) Digital photo showing the roots of hydroponically grown lettuce absorbing NIR-II fluorescent nanosensor. (b) Brightfield image of lettuce processed with the nanosensor under 808 nm laser excitation. (c) False-colored image of lettuce processed with the nanosensor under 808 nm laser excitation.

[Reviewer 3 comment 6] A comparative analysis with existing state-of-the-art sensors (not limited to other NIR sensors), particularly in terms of cost, sensitivity, and ease of deployment, is missing and would strengthen the study's relevance.

[Author Response]: We sincerely thank the reviewer for this constructive suggestion. Indeed, in addition to the NIR-II fluorescence sensors, there are currently visible light probes, genetically encoded probes, and electrochemical sensors available for monitoring plant stress. As the reviewer suggested, to provide a comprehensive understanding of the advancements and advantages of these advanced sensors, we have expanded our analysis to include a comparison with reported molecular probes, nanoprobes, genetically encoded probes, and electrochemical probes (**Supplemental Table 4**). Furthermore, in response to the valuable insights offered by Reviewer #3, we have also integrated the detection methods for various stress-related signaling molecules (such as ROS, phytohormones, and inorganic ions) with novel signal reporting strategies, as described in Supplementary Table 4. Through these comparative analyses, we aim to clarify the unique characteristics of NIR-II fluorescence nanosensors, as well as the characteristics of other methods concerning application

scenarios and monitoring capabilities, thereby providing a clearer view on the advantages of various sensors in plant stress monitoring. We have added these comparisons in the revised supporting information.

Supplementary Table 4. Representative sensors for detecting plant molecules associated with stress.

Sensing method	Analytes	Materials	Size	Plant species	Localization	Stress	LOD	Linear range	Refs
Optical	H_2O_2	H_2DCFDA	-	*Arabidopsis thaliana*	Whole plants	Light, wounding, pathogen	-	-	16
Optical	H_2O_2	2E2F	-	Malus hupehensis seedlings, 'Orin' apple calli, *Nicotiana benthamiana*	Calli, leaves	Wounding, high salinity, high light, drough	-	10-100 μM	17
Optical	H_2O_2	CT-XA-H_2O_2	-	Soybean, peanut	Sprouts	Cd^{2+}, high salinity	-	0-100 μM	18
Optical	H_2O_2	IXD-B	-	Mung bean, okra	Sprouts	Cd^{2+}	-	0-180 μM	19
Optical	H_2O_2	7,6 ss$(GT)_{15}$ SWCNT 6,5 ss$(AT)_{15}$ SWCNT	-	*Arabidopsis thaliana*	Leaves	-	-	-	20
Optical	H_2O_2	G-SWNT, A-SWNT	3.1 ± 0.1 nm (diameter) 613 ± 15 nm (length)	Lettuce, arugula, spinach, strawberry blite, sorrel, *Arabidopsis thaliana*	Leaves	Wounding, flg22, high light, high heat	55.7 μM (K_d)	-	4
Optical	H_2O_2	HeAptDNA-SWCNT	-	*Arabidopsis thaliana*	Leaves	UV-Blight, high light, flg22, wounding	-	0-1000 μM	21
Optical	H_2O_2	C_{20}/AgNC, FAM-C_{20}/AgNCs-Cy5	-	*Arabidopsis thaliana*, *Nicotiana benthamiana*	Roots, leaves	Pathogen	-	-	22
Optical	H_2O_2	AIE_{1035}NPs@Mo/Cu-POM	230 nm	*Arabidopsis thaliana*, lettuce, spinach, pepper, tobacco.	Leaves	Wounding, flg22, high heat	0.43 μM	1-40 μM	This work
Genetically encoded protein	H_2O_2	Hyper2	-	*Nicotiana benthamiana*	Whole plants	High light	-	-	23
Genetically encoded protein	H_2O_2	Hyper7	-	*Arabidopsis thaliana*	Whole plants	Pathogen, laser light	-	-	24
Genetically encoded protein	H_2O_2	roGFP2-Orp1	-	*Arabidopsis thaliana*	Whole plants	Pathogen	-	-	25
Electrochemical	H_2O_2	Nano-Au/ss	100 μm	Tomato	Stems	High salinity	3.97 μM	10-1000 μM	26
Electrochemical	H_2O_2	Hb/SWCNTs/CFUME	7 μm	Aloe	Leaves	High salinity	4 μM	4.90-405 μM	27
Electrochemical	H_2O_2	Nafion/Pt	1000 μm	Oilseed rape	Stems	Drought	1.24 μM	≤ 0.3mM	28
Electrochemical	H_2O_2	AuNPs/ITO	20 mm × 8 mm	Tomato	Leaves	Pathogen	-	0-1000 μM	29
Optical	H_2S	BSZ-H_2S	-	Rice	Roots	High salinity, drought	104 nM	0-140 μM	73
Optical	H_2S	HBTP-H_2S	-	Rice	Roots	Al^{3+}, flood	0.21μM	0-140 μM	74
Optical	H_2S	CHO-OH-NO_2	-	Wheat	Grains	Al^{3+}	0.75 μM	0-20 μM	75
Optical	SO_2	TPE-BA	-	Tobacco	Roots	Cd^{2+}	80.7 nM	0-100 μM	76
Genetically encoded protein	ABA	ABAleon2.1	-	*Arabidopsis thaliana*	Whole plants	Low humidity, salt stress, osmotic stress	79 nM	100-600 μM	77
Genetically encoded protein	ABA	ABACUS1-2μ, ABACUS1-80μ	-	*Arabidopsis thaliana*	Whole plants	Salt stress, osmotic stress	2 μM, 80 μM (K_d)	0.2-800 μM	78
Genetically encoded protein	ABA	nlsABACUS2–400n	-	*Arabidopsis thaliana*	Whole plants	Salt stress, low humidity	445 nM (K_d)	0.001-10 μM	79

Electrochemical	ABA	Au@SnO_2-VG/Ta	700 μm	Cucumber	Fruits	-	0.004 μM	0.012-495.2 μM	[80]
Genetically encoded protein	Auxin	Auxsen	-	*Arabidopsis thaliana*	Whole plants	Gravistimulation	-	10 nM-0.01 M	[81]
Optical	Auxin	SWNT	-	*Arabidopsis thaliana*, *Brassica rapa* subsp, pak choi, rice	Leaves	Herbicide	8.2μM (NAA), 0.35μM (2,4-D)	-	[82]
Electrochemical	Auxin	PST/Pt-ERGO/Au/ss	250 μm	Soybean	Stems	Salt stress	43 ng mL^{-1} (IAA)	0.1-100,000 ng mL^{-1}	[83]
Optical	GAs	GA-SWNT		*Arabidopsis thaliana*, lettuce, basil	Roots	Salt stress	542 nM (GA_3), 2.96 μM (GA_4)	0-150μM	[84]
Genetically encoded protein	GAs	nlsGPS1	-	*Arabidopsis thaliana*	Whole plants	-	110 nM (GA_1), 240 nM (GA_3), 24 nM (GA_4)	0.001-100 μM	[85]
Optical	SA	SWNT	-	*Arabidopsis thaliana*, Pak choi	Leaves	Wounding, pathogen, high light, high heat	4.4μM	1-500 μM	[62]
Electrochemical	SA	Digitalized pencil trace/ITO glass/ carbon tape	8 mm × 7 mm	*Arabidopsis thaliana*	Leaves	Leave detachment	-	1-100 μM	[86]
Electrochemical	SA	MWCNTS/Nafion/ carbon tape/ITO	12 mm × 7 mm	Tomato	Leaves	Pathogen	< 0.05 μM	0.5-100 μM	[87]
Electrochemical	SA	MWCNT/SPE	4 mm	Basil	Leaves	-	-	0-10 mM	[88]
Electrochemical	SA	NDG microelectrode	300 μm	Cucumber	Stems	-	0.14 μM	1-500 μM	[89]
Electrochemical	SA	Pt nanoflowers/ERGO /Pt	500 μm	Sunflower seedlings	Stems	Salt stress	3.3 pM	10 pM-500 nM	[90]
Electrochemical	SA	Magnetic MIPs/MN/IDEs	70 μm	*Arabidopsis thaliana*, *Nicotiana benthamiana*	Leaves	Pathogen	2.74 μM	≤ 150 μM	[91]
Electrochemical	SA	Au@Cu_2O/Gr/PDA /IDME	250 μm	Cucumber	Leaves	-	1.16 nM	0.01-1.04/1.04-100 μM	[92]
Optical	Isoprene	DMIC	-	*Arabidopsis thaliana*	Leaves	Salt stress, high temperature	1.6 ppm	1-560 ppm	[93]
Optical	ATP	IR-1061 micelle@ZIF-90	266.1 nm	Spinach	Leaves	Wounding	7.06 μM	0-100 μM	[94]
Genetically encoded protein	ATP	ATeam1.03-nD/nA	-	*Arabidopsis thaliana*	Whole plants	-	50 μM (K_d)	-	[95]
Genetically encoded protein	Ca^{2+}	Aequorin	-	*Arabidopsis thaliana*, rice	Whole plants	Salt stress, H_2O_2	-	-	[96]
Genetically encoded protein	Ca^{2+}	CGf	-	*Arabidopsis thaliana*	Whole plants	Heat, blue light stress	203-223 nM (K_d)	0.017-39 μM	[97]
Genetically encoded protein	Ca^{2+}	G5A	-	*Arabidopsis thaliana*	Whole plants	Dark stress, salt stress	-	10-1000 nM	[98]
Genetically encoded protein	Ca^{2+}	GCaMP6s	-	*Arabidopsis thaliana*	Whole plants	Wounding, glutamate	-	-	[99]
Genetically encoded protein	Ca^{2+}	ER-GCaMP6-210	-	*Arabidopsis thaliana*	Whole plants	ATP, wounding	210 nM (K_d)	-	[100]

Abbreviations: ABA, abscisic acid; ATP, adenosine-5'-triphosphate; Ca^{2+}, calcium ions; Cd^{2+}, cadmium ions; GAs, gibberellins; H_2DCFDA, 2',7'-dichlorofluorescin diacetate; H_2O_2, hydrogen peroxide; K_d, dissociation constant; IAA, indole-3-acetic acid; LOD, limit of detection; NAA, 1-naphthalene acetic acid; SA, salicylic acid; SO_2, sulfur dioxide; 2,4-D, 2,4-dichlorophenoxyacetic acid; SWCNT/SWNT, single-wall carbon nanotube.

[Reviewer 3 comment 7] How does the nanosensor perform under open-field conditions with fluctuating environmental factors such as humidity, wind, and soil variability?

[Author Response]: We thank the reviewer for the insightful comment. Under open-field conditions, environmental factors such as humidity, wind, and soil conditions fluctuate, making the performance of the nanosensor in variable environments crucial for its practical application in agricultural monitoring. Currently, our developed sensor is primarily designed for greenhouse applications. To assess its adaptability to different environmental factors, we conducted experiments under varying air humidity (40%~60%) and different soil moisture levels (35% on the day of watering and 20% on the third day after watering), as well as under fertilized and non-fertilized conditions (Supplementary Fig. 37). The nanosensors demonstrated a sensitive response to the stress state of the plants under varying air humidity conditions. Although changes in soil moisture content may affect the overall physiological state of the plant, the sensor's ability to detect H_2O_2 signals in the plant was not significantly disturbed, as it is not directly affected by soil conditions. Furthermore, the sensor effectively distinguished between the stress states of plants under fertilized and non-fertilized conditions, indicating its suitability for different greenhouse management strategies. We have added these experimental results in the revised manuscript to further highlight the sensor's potential for use in a variety of greenhouse conditions. The revisions are as follows:

"In addition, the nanosensor can effectively monitor the stress status of plants under varying air humidity, soil moisture, and fertilization conditions, demonstrating its applicability to diverse greenhouse management strategies (Supplementary Fig. 37, 38)." (Page 13, line 263-265 in revised manuscript)

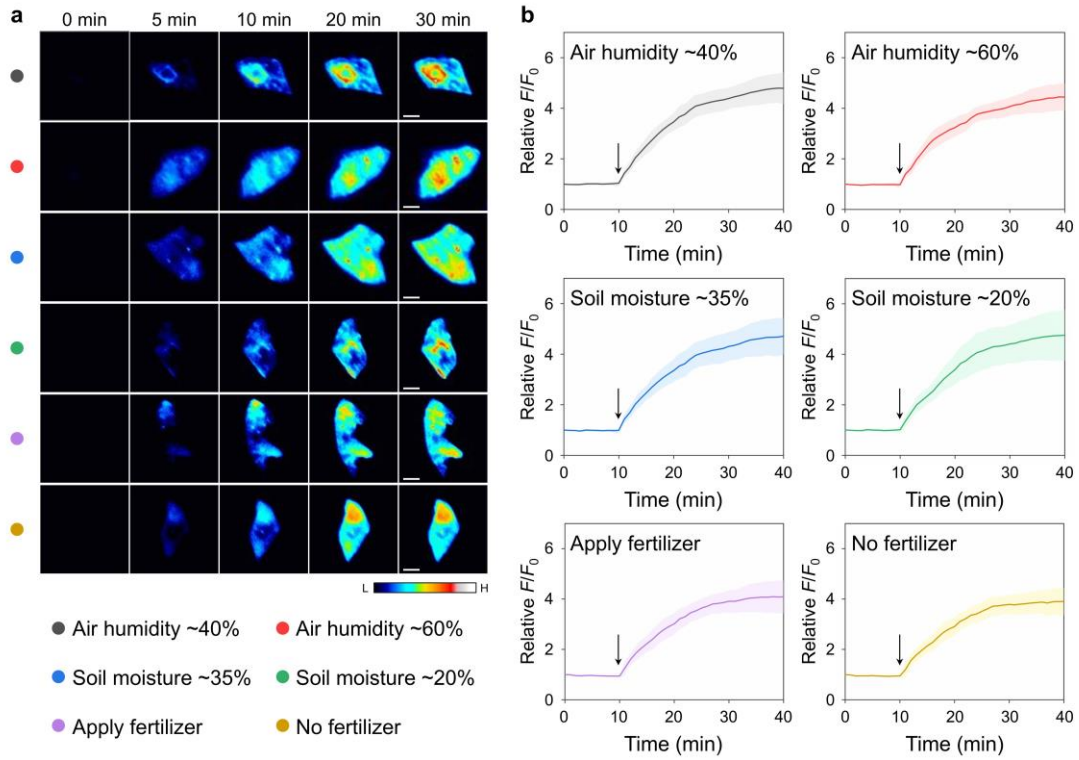

Supplementary Fig. 37. Performance of nanosensors in monitoring plant stress signals under different greenhouse environments. (a) NIR fluorescence images of AIE$_{1035}$NPs@Mo/Cu-POM nanosensor response towards H_2O_2 induced by wounding in plants. The time denotes the time points following wounding. Scale bar: 5 mm. (b) Time profiles of normalized fluorescence intensity of AIE$_{1035}$NPs@Mo/Cu-POM throughout the experiment. The black arrow indicates the time of wounding. Shaded regions represent the standard error across three independent measurements.

[Reviewer 3 comment 8] What is the estimated lifespan of the nanosensors when deployed on plants? Are the sensors reusable, or are they intended for single use?

[Author Response]: We thank the reviewer for the insightful comments. Many plant stress signals, such as ROS and Ca^{2+}, are rapidly produced within minutes to hours after stress occurs and propagate between cells. As key indicators of a plant's early defense response, these signals provide critical insights into initial stress adaptation. Therefore, monitoring their short-term dynamics allows for a clearer understanding of how plants respond to stress at the earliest stages. Recent studies on advanced nanosensors have primarily focused on the short-term (a few hours) stress responses in plants, as reported in *Nat. Commun.* 15, 2943 (2024)[62]; *Nat. Nanotechnol.* 18, 205–216 (2023)[61]; *Nat.*

Plants 6, 404–415 (2020)[4]; *Nano Lett.* 23, 916–924 (2023)[84], which is related to the time-sensitivity of early plant stress signals.

The nanosensor developed in this study are designed for single-use applications, primarily focusing on the early detection of H_2O_2 production as a stress response in plants. To further assess the performance of the nanosensor, we evaluated its sensing capability in plants for 4 hours. The results indicate that the nanosensor maintains a stable response to H_2O_2, despite the complex internal environment of the plant (Supplementary Fig. 38). We are currently exploring the integration of nanosensors with microneedle patches and flexible fiber-based platforms to extend their monitoring capabilities for several days. This approach could enable long-term stress monitoring while maintaining the advantages of real-time, non-destructive detection.

We have made corresponding changes to this part in the revised supporting information.

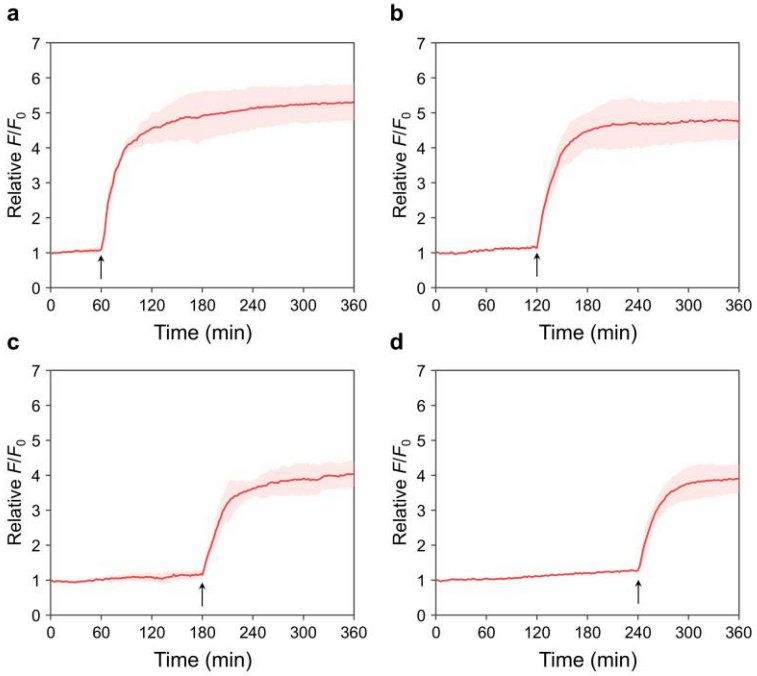

Supplementary Fig. 38. Performance of nanosensors in monitoring plant stress signals over a period of 4 hours. After the plant leaves were injected with nanosensors, scratches were made on the leaves at one hour (a), two hours (b), three hours (c), and four hours (d) to continuously monitor the fluorescence changes of the nanosensors. The black arrow indicates the time of wounding, while the shaded regions represent the standard error across three independent measurements.

[Reviewer 3 comment 9] Could this nanosensor technology be adapted to detect other plant signaling molecules, potentially broadening its applicability to other agricultural or environmental diagnostics?

[Author Response]: We thank the reviewer for the insightful question. The NIR-II fluorescent nanosensor developed in our study is designed to detect plant signaling molecules with high sensitivity and specificity. In addition to H_2O_2, similar nanosensor platforms have demonstrated their capability to monitor other essential signaling molecules in plants, such as phytohormones (*Nat. Commun.* 15, 2943 (2024)[62]; *Nano Lett.* 23, 916–924 (2023)[84]; *ACS Sens.* 6, 3032–3046 (2021)[82]), polyphenols (*Angew. Chem. Int. Ed.,* 61 e202108373 (2022)[101]), and nitric oxide (*Small* 11, 3973-3984 (2015)[20], *Nat. Mater.* 13, 400-408 (2014)[102]). Recent studies have successfully utilized NIR-II nanosensors to detect these molecules, highlighting their versatility in monitoring plant stress. In our research group, we are actively exploring the potential to extend this nanosensor technology to other signaling molecules related to plant stress, such as adenosine 5'-triphosphate (ATP) and hydrogen sulfide (H_2S), which play a vital role in plant stress responses. These advancements would broaden the applicability of our nanosensor, making it a versatile tool for agricultural and environmental diagnostics. The nanosensor's species-independent nature and real-time monitoring capabilities position it as a promising candidate for comprehensive assessments of plant health. Future efforts will focus on optimizing sensor specificity and sensitivity for a wider range of biomolecules to facilitate precise and early detection of stress in plants.

References

1 Mittler, R. Oxidative stress, antioxidants and stress tolerance. *Trends Plant Sci.* **7**, 405-410 (2002).

2 Reth, M. Hydrogen peroxide as second messenger in lymphocyte activation. *Nat. Immunol.* **3**, 1129-1134 (2002).

3 Smirnoff, N. & Arnaud, D. Hydrogen peroxide metabolism and functions in plants. *New Phytol.* **221**, 1197-1214 (2019).

4 Lew, T. T. S. *et al.* Real-time detection of wound-induced H_2O_2 signalling waves in plants with optical nanosensors. *Nat. Plants.* **6**, 404-415 (2020).

5 Wang, Y. *et al.* GSH and H_2O_2 dynamic correlation in the ferroptosis pathways revealed by engineered probe in tumor and kidney injury. *Chem. Eng. J.* **464**, 142496 (2023).

6 Zan, Q. *et al.* Mitochondria-targetable near-infrared fluorescent probe for visualization of hydrogen peroxide in lung injury, liver injury, and tumor models. *Anal. Chem.* **96**, 10488-10495 (2024).

7 Chen, J. *et al.* A H_2O_2-activatable nanoprobe for diagnosing interstitial cystitis and liver ischemia-reperfusion injury via multispectral optoacoustic tomography and NIR-II fluorescent imaging. *Nat. Commun.* **12**, 6870 (2021).

8 Chen, Y. *et al.* A promising NIR-II fluorescent sensor for peptide-mediated long-term monitoring of kidney dysfunction. *Angew. Chem. Int. Ed.* **60**, 15809-15815 (2021).

9 Zhang, X. *et al.* Plasmonic-fluorescent Janus Ag/Ag_2S nanoparticles for in situ H_2O_2-activated NIR-II fluorescence imaging. *Nano Lett.* **21**, 2625-2633 (2021).

10 Zhan, Y. *et al.* Activatable NIR-II lanthanides-polymetallic oxomolybdate hybrid nanosensors for monitoring chemotherapy induced enteritis. *Adv. Funct. Mater.* **33**, 2301683 (2023).

11 Zeng, Z., Chen, J., Sun, L., Zeng, F. & Wu, S. A biomarker-responsive nanoprobe for detecting hepatic ischemia-reperfusion injury via optoacoustic/NIR-II fluorescence imaging. *Chem. Commun.* **59**, 571-574 (2023).

12 Ledesma, F. *et al.* Covalent attachment of horseradish peroxidase to single-walled carbon nanotubes for hydrogen peroxide detection. *Adv. Funct. Mater.*, 2316028 (2024).

13 Li, Y. *et al.* Design of AIEgens for near-infrared IIb imaging through structural modulation at molecular and morphological levels. *Nat. Commun.* **11**, 1255 (2020).

14 Liu, S. *et al.* Molecular motion in aggregates: manipulating TICT for boosting photothermal theranostics. *J. Am. Chem. Soc.* **141**, 5359-5368 (2019).

15 Chen, Y., Wang, S. & Zhang, F. Near-infrared luminescence high-contrast *in vivo* biomedical imaging. *Nat. Rev. Bioeng.* **1**, 60-78 (2023).

16 Fichman, Y., Miller, G. & Mittler, R. Whole-plant live imaging of reactive oxygen species. *Mol. Plant* **12**, 1203-1210 (2019).

17 Yin, Y. *et al.* Simple phenotypic sensor for visibly tracking H_2O_2 fluctuation to

detect plant health status. *J. Agric. Food Chem.* **70**, 10058-10064 (2022).
18 Long, Y., Chen, J., Zeng, F. & Wu, S. An activatable NIR-II fluorescent probe for tracking heavy-metal ion and high-level salt-induced oxidative stress in plant sprouts. *Aggregate* **4**, 4:e288 (2022).
19 Zeng, C., Long, Y., Tan, Y., Zeng, F. & Wu, S. Water-dispersible activatable nanoprobe for detecting cadmium-ion-induced oxidative stress in edible crops via near-infrared second-window fluorescence imaging. *Anal. Chem.* **94**, 14021-14028 (2022).
20 Giraldo, J. P. *et al.* A ratiometric sensor using single chirality near-infrared fluorescent carbon nanotubes: application to *in vivo* monitoring. *Small* **11**, 3973-3984 (2015).
21 Wu, H. *et al.* Monitoring plant health with near-infrared fluorescent H_2O_2 nanosensors. *Nano Lett.* **20**, 2432-2442 (2020).
22 Oh, Y. K. *et al.* Application of fluorescence i-motif DNA silver nanocluster sensor to visualize endogenous reactive oxygen species in plant cells. *Plant Cell Rep.* **44**, 6 (2024).
23 Exposito-Rodriguez, M., Laissue, P. P., Yvon-Durocher, G., Smirnoff, N. & Mullineaux, P. M. Photosynthesis-dependent H_2O_2 transfer from chloroplasts to nuclei provides a high-light signalling mechanism. *Nat. Commun.* **8**, 49 (2017).
24 Ugalde, J. M., Schlößer, M., Dongois, A., Martinière, A. & Meyer, A. J. The latest HyPe(r) in plant H_2O_2 biosensing. *Plant. Physiol.* **187**, 480-484 (2021).
25 Nietzel, T. *et al.* The fluorescent protein sensor roGFP2-Orp1 monitors *in vivo* H_2O_2 and thiol redox integration and elucidates intracellular H_2O_2 dynamics during elicitor-induced oxidative burst in *Arabidopsis*. *New Phytol.* **221**, 1649-1664 (2019).
26 Huo, D. *et al.* Disposable stainless-steel wire-based electrochemical microsensor for *in vivo* continuous monitoring of hydrogen peroxide in vein of tomato leaf. *Biosensors* **12**, 35 (2022).
27 Ren, Q.-Q. *et al. In vivo* monitoring of oxidative burst on aloe under salinity stress using hemoglobin and single-walled carbon nanotubes modified carbon fiber ultramicroelectrode. *Biosens. Bioelectron.* **50**, 318-324 (2013).
28 Ren, Q.-Q. *et al.* A field-compatible technique using an electrochemical sensing microbundle for real-time and simultaneous *in vivo* measurement of hydrogen peroxide, nitric oxide, and pH under drought stress. *Sens. Actuat. B Chem.* **220**, 743-748 (2015).
29 Sun, L. *et al.* Paper-based analytical devices for the rapid and direct electrochemical detection of hydrogen peroxide in tomato leaves inoculated with botrytis cinerea. *Sensors* **20**, 5512 (2020).
30 Mittler, R., Zandalinas, S. I., Fichman, Y. & Van Breusegem, F. Reactive oxygen species signalling in plant stress responses. *Nat. Rev. Mol. Cell. Bio.* **23**, 663-679 (2022).
31 Sies, H. & Jones, D. P. Reactive oxygen species (ROS) as pleiotropic physiological signalling agents. *Nat. Rev. Mol. Cell Biol.* **21**, 363-383 (2020).
32 Schwarzländer, M., Fricker, M. D. & Sweetlove, L. J. Monitoring the *in vivo*

redox state of plant mitochondria: Effect of respiratory inhibitors, abiotic stress and assessment of recovery from oxidative challenge. *Biochim. Biophys. Acta, Bioenerg.* **1787**, 468-475 (2009).

33 Kámán-Tóth, E. *et al.* Contribution of cell wall peroxidase- and NADPH oxidase-derived reactive oxygen species to Alternaria brassicicola-induced oxidative burst in Arabidopsis. *Mol. Plant Pathol.* **20**, 485-499 (2019).

34 Torres, M. A., Dangl, J. L. & Jones, J. D. G. Arabidopsis gp^{91} phox homologues AtrbohD and AtrbohF are required for accumulation of reactive oxygen intermediates in the plant defense response. *Proc. Natl Acad. Sci. USA* **99**, 517-522 (2001).

35 Das, R. & Bhattacharjee, C. Lettuce in Nutritional composition and antioxidant properties of fruits and vegetables, Academic Press, pp. 143-157 (2020).

36 Bhattarai, G. & Shi, A. Research advances and prospects of spinach breeding, genetics, and genomics. *Veg. Res.* **1**, 1-18 (2021).

37 Jassbi, A. R., Zare, S., Asadollahi, M. & Schuman, M. C. Ecological roles and biological activities of specialized metabolites from the genus *Nicotiana*. *Chem. Rev.* **117**, 12227-12280 (2017).

38 Barik, S. *et al.* A critical insight into the breeding for resistance to bacterial diseases in pepper (*Capsicum* spp.). *J. Crop Health* **76**, 957-979 (2024).

39 Zhao, H. *et al.* A polyoxometalate-based pathologically activated assay for efficient bioorthogonal catalytic selective therapy. *Angew. Chem. Int. Ed.* **62**, e202303989 (2023).

40 Gumerova, N. I. & Rompel, A. Synthesis, structures and applications of electron-rich polyoxometalates. *Nat. Rev. Chem.* **2**, 0112 (2018).

41 Weinstock, I. A., Schreiber, R. E. & Neumann, R. Dioxygen in polyoxometalate mediated reactions. *Chem. Rev.* **118**, 2680-2717 (2017).

42 Cheng, H., Kamegawa, T., Mori, K. & Yamashita, H. Surfactant-free nonaqueous synthesis of plasmonic molybdenum oxide nanosheets with enhanced catalytic activity for hydrogen generation from ammonia borane under visible light. *Angew. Chem. Int. Ed.* **53**, 2910-2914 (2014).

43 Zhang, C. *et al.* A polyoxometalate cluster paradigm with self-adaptive electronic structure for acidity/reducibility-specific photothermal conversion. *J. Am. Chem. Soc.* **138**, 8156-8164 (2016).

44 Carlson, L. J., Maccagnano, S. E., Zheng, M., Silcox, J. & Krauss, T. D. Fluorescence efficiency of iIndividual carbon nanotubes. *Nano Lett.* **7**, 3698-3703 (2007).

45 Antaris, A. L. *et al.* A small-molecule dye for NIR-II imaging. *Nat. Mater.* **15**, 235-242 (2015).

46 Bhattacharjee, S. DLS and zeta potential – What they are and what they are not? *J. Controlled Release* **235**, 337-351 (2016).

47 Lee, G. *et al.* Abaxial leaf surface-mounted multimodal wearable sensor for continuous plant physiology monitoring. *Sci. Adv.* **9**, eade2232 (2023).

48 Yang, Y. *et al.* All-organic transparent plant e-skin for noninvasive phenotyping. *Sci. Adv.* **10**, eadk7488 (2024).

49 Coatsworth, P. *et al.* Time-resolved chemical monitoring of whole plant roots with printed electrochemical sensors and machine learning. *Sci. Adv.* **10**, eadj6315 (2024).

50 Zhou, J., Fan, P., Zhou, S., Pan, Y. & Ping, J. Machine learning-assisted implantable plant electrophysiology microneedle sensor for plant stress monitoring. *Biosens. Bioelectron.* **271**, 117062 (2025).

51 Khait, I. *et al.* Sounds emitted by plants under stress are airborne and informative. *Cell* **186**, 1328-1336.e1310 (2023).

52 Sharma, P., Jha, A. B., Dubey, R. S. & Pessarakli, M. Reactive oxygen species, oxidative damage, and antioxidative defense mechanism in plants under stressful conditions. *J. Bot.* **2012**, 1-26 (2012).

53 Tian, Y. *et al.* Hydrogen peroxide positively regulates brassinosteroid signaling through oxidation of the BRASSINAZOLE-RESISTANT1 transcription factor. *Nat. Commun.* **9**, 1063 (2018).

54 Cerny, M., Habanova, H., Berka, M., Luklova, M. & Brzobohaty, B. Hydrogen peroxide: its role in plant biology and crosstalk with signalling networks. *Int. J. Mol. Sci.* **19**, 2812 (2018).

55 Waszczak, C., Carmody, M. & Kangasjarvi, J. Reactive oxygen species in plant signaling. *Annu. Rev. Plant. Biol.* **69**, 209-236 (2018).

56 Romero-Puertas, M. C. *et al.* Cadmium-induced subcellular accumulation of $O_2^{\cdot-}$ and H_2O_2 in pea leaves. *Plant Cell Environ.* **27**, 1122-1134 (2004).

57 Orozco-Cardenas, M. & Ryan, C. A. Hydrogen peroxide is generated systemically in plant leaves by wounding and systemin via the octadecanoid pathway. *Proc. Natl Acad. Sci. USA* **96**, 6553-6557 (1999).

58 Mullineaux, P. M., Karpinski, S. & Baker, N. R. Spatial dependence for hydrogen peroxide-directed signaling in light-stressed plants. *Plant. Physiol.* **141**, 346-350 (2006).

59 Miller, G. *et al.* The plant NADPH oxidase RBOHD mediates rapid systemic signaling in response to diverse stimuli. *Sci. Signaling* **2**, ra45 (2009).

60 Exposito-Rodriguez, M., Laissue, P. P., Littlejohn, G. R., Smirnoff, N. & Mullineaux, P. M. The use of HyPer to examine spatial and temporal changes in H_2O_2 in high light-exposed plants. *Methods Enzymol.* **527**, 185-201 (2013).

61 Son, W. K. *et al. In vivo* surface-enhanced Raman scattering nanosensor for the real-time monitoring of multiple stress signalling molecules in plants. *Nat. Nanotechnol.* **18**, 205-216 (2022).

62 Ang, M. C. *et al.* Decoding early stress signaling waves in living plants using nanosensor multiplexing. *Nat. Commun.* **15**, 2943 (2024).

63 Giraldo, J. P., Wu, H., Newkirk, G. M. & Kruss, S. Nanobiotechnology approaches for engineering smart plant sensors. *Nat. Nanotechnol.* **14**, 541-553 (2019).

64 Zhang, M. *et al.* Nanomaterials: recent advances in plant disease diagnosis and treatment. *Nano Today* **57** (2024).

65 Wong, M. H. *et al.* Nitroaromatic detection and infrared communication from wild-type plants using plant nanobionics. *Nat. Mater.* **16**, 264-272 (2017).

66 Lew, T. T. S., Park, M., Cui, J. & Strano, M. S. Plant Nanobionic Sensors for Arsenic Detection. *Adv. Mater.* **33**, 2005683 (2021).
67 Wang, S. *et al.* Sunflower-like self-sustainable plant-wearable sensing probe. *Sci. Adv.* **10**, eads1136 (2024).
68 Armada-Moreira, A. *et al.* Plant electrophysiology with conformable organic electronics: Deciphering the propagation of Venus flytrap action potentials. *Sci. Adv.* **9**, eadh4443 (2023).
69 Liu, C. *et al.* A self-powered dual ratchet angle sensing system for digital twins and smart healthcare. *Adv. Funct. Mater.* **34**, 2405104 (2024).
70 Maaten, L. v. d. & Hinton, G. Visualizing data using t-SNE. *J. Mach. Learn. Res.* **9**, 2579-2605 (2008).
71 Wang, S. *et al.* Chromatic covalent organic frameworks enabling in-vivo chemical tomography. *Nat. Commun.* **15**, 2943 (2024).
72 Wu, X. *et al.* Rapid and in-field sensing of hydrogen peroxide in plant by hydrogel microneedle patch. *Small* **20**, 2402024 (2024).
73 Lin, Y.-M. *et al.* Near-infrared fluorescent probe for imaging upregulated hydrogen sulfide levels in rice under salt and drought stress. *J. Agric. Food Chem.* **71**, 5154-5161 (2023).
74 Wang, J. *et al.* NIR fluorescent probe for in situ bioimaging of endogenous H_2S in rice roots under Al^{3+} and flooding stresses. *J. Agric. Food Chem.* **69**, 14330-14339 (2021).
75 Liang, K., Li, Y., Zeng, F. & Wu, S. A near-infrared fluorescent probe for detection of H_2S and its application in monitoring meat freshness and plant growth under aluminium-induced stress. *New J. Chem.* **47**, 2643-2650 (2023).
76 Zhang, S. *et al.* An ICT-based ratiometric fluorescent probe for tracking and imaging SO_2 during Cd-induced stress in plants. *Sens. Actuat. B Chem.* **395** (2023).
77 Waadt, R. *et al.* FRET-based reporters for the direct visualization of abscisic acid concentration changes and distribution in Arabidopsis. *eLife* **3**, e01739 (2014).
78 Jones, A. M. *et al.* Abscisic acid dynamics in roots detected with genetically encoded FRET sensors. *eLife* **3**, e01741 (2014).
79 Rowe, J. *et al.* Next-generation ABACUS biosensors reveal cellular ABA dynamics driving root growth at low aerial humidity. *Nat. Plants.* **9**, 1103-1115 (2023).
80 Wang, Z. *et al.* Au@SnO_2-vertical graphene-based microneedle sensor for in-situ determination of abscisic acid in plants. *Mater. Sci. Eng. C* **127**, 112237 (2021).
81 Herud-Sikimić, O. *et al.* A biosensor for the direct visualization of auxin. *Nature* **592**, 768-772 (2021).
82 Ang, M. C. *et al.* Nanosensor detection of synthetic auxins in planta using corona phase molecular recognition. *ACS Sens.* **6**, 3032-3046 (2021).
83 Li, H. *et al.* Disposable stainless steel-based electrochemical microsensor for *in vivo* determination of indole-3-acetic acid in soybean seedlings. *Biosens.*

Bioelectron. **126**, 193-199 (2019).
84 Boonyaves, K. *et al.* Near-infrared fluorescent carbon nanotube sensors for the plant hormone family gibberellins. *Nano Lett.* **23**, 916-924 (2023).
85 Rizza, A., Walia, A., Lanquar, V., Frommer, W. B. & Jones, A. M. *In vivo* gibberellin gradients visualized in rapidly elongating tissues. *Nat. Plants.* **3**, 803-813 (2017).
86 He, K.-C. *et al.* Digitalized pencil trace modified electrodes for real time evaluation of salicylic acid in detached Arabidopsis thaliana leaves during regeneration. *Anal. Chim. Acta* **1120**, 59-66 (2020).
87 Sun, L.-J. *et al.* Paper-based electroanalytical devices for in situ determination of salicylic acid in living tomato leaves. *Biosens. Bioelectron.* **60**, 154-160 (2014).
88 González-Sánchez, M. I., Lee, P. T., Guy, R. H. & Compton, R. G. In situ detection of salicylate in Ocimum basilicum plant leaves via reverse iontophoresis. *Chem. Commun.* **51**, 16534-16536 (2015).
89 Zhang, F. *et al.* Fabrication of self-supporting nitrogen-doped graphene microelectrodes for in situ analysis of salicylic acid in plants. *Carbon* **175**, 364-376 (2021).
90 Hu, Y. *et al. In vivo* detection of salicylic acid in sunflower seedlings under salt stress. *RSC Adv.* **8**, 23404-23410 (2018).
91 Bukhamsin, A. *et al.* Minimally-invasive, real-time, non-destructive, species-independent phytohormone biosensor for precision farming. *Biosens. Bioelectron.* **214** (2022).
92 Liu, D. *et al.* Core-shell Au@Cu_2O-graphene-polydopamine interdigitated microelectrode array sensor for in situ determination of salicylic acid in cucumber leaves. *Sens. Actuat. B Chem.* **341**, 130027 (2021).
93 Liu, Z. *et al.* A sensitive coumarin fluorescence sensor designed for isoprene detection and imaging research in plants. *Biosens. Bioelectron.* **248**, 115998 (2024).
94 Qiu, Q. *et al.* Second near-infrared fluorescent metal-organic framework sensors for *in vivo* extracellular adenosine triphosphate monitoring. *Biosens. Bioelectron.* **251**, 116114 (2024).
95 Voon, C. P. *et al.* ATP compartmentation in plastids and cytosol of *Arabidopsis thaliana* revealed by fluorescent protein sensing. *Proc. Natl Acad. Sci. USA* **115**, 10778-10787 (2018).
96 Zhang, Y. *et al.* Aequorin-based luminescence imaging reveals differential calcium signalling responses to salt and reactive oxygen species in rice roots. *J. Exp. Bot.* **66**, 2535-2545 (2015).
97 Weigand, C. *et al.* A ratiometric calcium reporter CGf reveals calcium dynamics both in the single cell and whole plant levels under heat stress. *Front. Plant Sci.* **12**, 777975 (2021).
98 Xiong, T. C. *et al.* Imaging long distance propagating calcium signals in intact plant leaves with the BRET-based GFP-aequorin reporter. *Front. Plant Sci.* **5**, 43 (2014).

99 Shao, Q., Gao, Q., Lhamo, D., Zhang, H. & Luan, S. Two glutamate- and pH-regulated Ca^{2+} channels are required for systemic wound signaling in *Arabidopsis*. *Sci. Signaling* **13**, eaba1453 (2020).

100 Resentini, F. *et al.* Simultaneous imaging of ER and cytosolic Ca^{2+} dynamics reveals long-distance ER Ca^{2+} waves in plants. *Plant. Physiol.* **187**, 603-617 (2021).

101 Nissler, R. *et al.* Detection and imaging of the plant pathogen response by near-Iinfrared fluorescent polyphenol sensors. *Angew. Chem. Int. Ed.* **61**, e202108373 (2022).

102 Giraldo, J. P. *et al.* Plant nanobionics approach to augment photosynthesis and biochemical sensing. *Nat. Mater.* **13**, 400-408 (2014).

Responses to Reviewers' Comments:

First and foremost, we would like to express our gratitude to the reviewers for their time and effort during the review process. The reviewers' insightful comments and suggestions have significantly enhanced the quality and clarity of our manuscript. We are grateful to the reviewers for their comments on our manuscript. Below, we present our point-by-point responses to the comments revised in the second round of review.

Reviewer #1 (Remarks to the Author)

I am satisfied with the authors' revisions and do not have further comments. I believe it can be considered for publication in Nature Communications now.

[Author Response]: We are delighted to receive your positive comments. Thank you very much for reviewing our article. Your insightful comments greatly improve and strengthen our work.

Reviewer #2 (Remarks to the Author)

I co-reviewed this manuscript with one of the reviewers who provided the listed reports. This is part of the Nature Communications initiative to facilitate training in peer review and to provide appropriate recognition for Early Career Researchers who co-review manuscripts.

[Author Response]: Thank you for reviewing our manuscript. We sincerely appreciate the effort that you and your co-reviewer have dedicated to the review process.

Reviewer #3 (Remarks to the Author)

I appreciate the thorough and thoughtful responses to my previous comments. The authors have clearly made substantial revisions to the manuscript, including additional experimental data, expanded discussion on scalability and environmental impact, and a much more comprehensive treatment of the machine learning implementation. These improvements significantly strengthen the manuscript.

As a suggestion to further enhance clarity for readers interested in real-world applications, it might be helpful to include a schematic or dedicated paragraph outlining

the envisioned field deployment workflow — from nanosensor administration to signal acquisition and ML-based classification. This would help bridge the gap between lab-based validation and practical agricultural use cases.

That aside, I have no further concerns, and I believe the paper is now suitable for publication.

[Author Response]: Thank you very much for your kindness and assistance in enhancing our work. We are honored to have your approval of our revised article.

We have added a dedicated paragraph that describes the entire pipeline—from the administration of nanosensor and signal acquisition using imaging devices to stress classification through the ML model. This addition offers a clearer roadmap for translating lab-based validation into real-world agricultural monitoring scenarios. Furthermore, a schematic diagram (Supplementary Fig. 47) has been included to visually summarize this workflow. The revised content is as follows:

"To facilitate field deployment, a conceptual workflow has been outlined to illustrate the transition from laboratory-based validation to real-world application (Supplementary Fig. 47)." (Page 21, line 419-421 in revised manuscript)

"To meet the practical needs of agricultural applications, we have developed an optimized workflow that is adaptable to both laboratory and field environments. For laboratory validation (Supplementary Fig. 47a), the nanosensors were initially infiltrated into plant leaves using a needleless syringe, and any residual liquid was subsequently washed off. Following a 1-hour incubation period, images were continuously captured using a custom NIR-II imaging system, which was equipped with an 808 nm excitation laser and appropriate long-pass filters, at a fixed sampling frequency (T = 20 s). The probe injection site in the plant served as the fixed location for signal extraction, and NIR-II signals were extracted for 1 h to generate the raw time series data. After denoising and normalization, the datasets were summarized and input into the ML model for plant stress recognition.

For field applications (Supplementary Fig. 47b), the nanosensors were manually administered to the plant leaves using a needle-free syringe. To minimize interference

from ambient light in outdoor environments, imaging was conducted within a temporary light-shielding setup, such as a portable blackout tent or a custom shade box. Fluorescence signals from the sensor-infiltrated leaves were acquired using a portable, miniaturized infrared camera. The imaging device was either handheld or mounted on a tripod to ensure stability and was used to capture images at fixed intervals (e.g., every 10-60 s) over a specified monitoring period (e.g., 30-60 min). The captured images were transmitted in real-time to a single-board computer (e.g., Raspberry Pi) and underwent onboard preprocessing, which included noise reduction, background subtraction, and normalization to generate analyzable fluorescence signal curves. An embedded ML model (e.g., XGBoost) trained on a pre-validated dataset was deployed on the single-board computer. The standardized fluorescence datasets were input into the model to enable real-time classification of plant stress states (e.g., no stress, heat stress, pathogen-induced stress, mechanical damage). The classification results were displayed via a connected interface or transmitted wirelessly for remote monitoring."

(Supplementary Note 21: Laboratory and field deployment workflow)

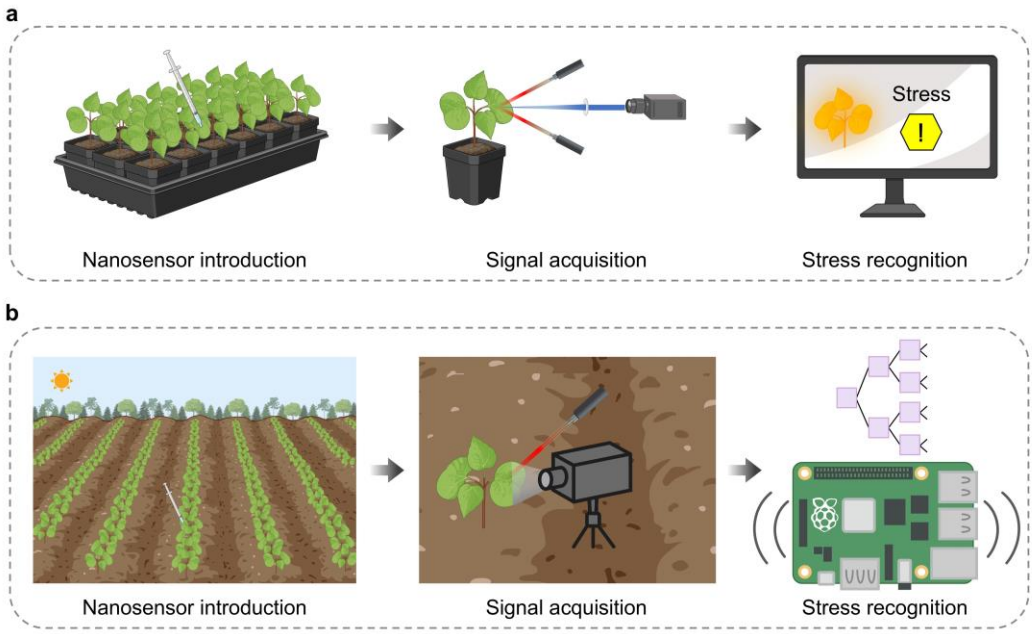

Supplementary Fig. 47. Deployment workflow for NIR-II nanosensor-based plant stress monitoring. a, Schematic diagram of the laboratory validation workflow for the plant stress monitoring. b, Schematic diagram of the field deployment workflow for the plant stress monitoring. Created in BioRender. Hu, H. (2025)

https://BioRender.com/hcf1nsf.

Comments to the Author

Comments on the manuscript with ID: NCOMMS-24-81227, whose title is “Machine learning-powered activatable NIR-II fluorescent nanosensor for in vivo monitoring of plant stress responses”.

In this study, Wang and coworkers present a novel NIR-II fluorescent nanosensor for real-time, non-destructive monitoring of H_2O_2 signaling in living plants, demonstrating its impressive sensitivity and species-independence as a reliable means for the real-time report of stress information. Further, the integration with machine learning model for stress classification further highlights its potential in precision agriculture. Overall, the reviewer finds the present study is well organized and possesses certain innovation and practical application value. I believe major revisions are required before this manuscript can be finally published.

The following issues should be addressed:

1. In the introduction, it is necessary to elaborate on the unique advantages and core contributions of the proposed nanosensor compared to existing NIR-II fluorescence-based technologies. For example, (i) how does the performance of the proposed sensor compared to other state-of-the-art NIR-II sensors in terms of sensitivity, selectivity, and real-time response capability? As known, the synthesized NIR-II molecular probe in this work is already reported and characterized by Tang and coworkers, Nature Communications 11, 1255 (2020), J. Am. Chem. Soc. 2019, 141, 13, 5359.
2. (ii) Considering the fact that NIR-II imaging is widely utilized in precision medical diagnosis and treatment, when the application scenario switches to plants stress monitoring, what are the similarities and differences between them, such as depth of penetration or fluorescence wavelengths and etc.
3. In addition, while the manuscript emphasizes the sensor's broad applicability to various plant species, it would be valuable to discuss whether its detection sensitivity or specificity surpasses that of previously reported methods.
4. Regarding the dataset used for the machine learning model, it is recommended to include details on its composition in the main text. Information such as the distribution of fluorescence intensity levels, stress conditions, and plant species within the dataset would provide a clearer understanding of its structure. Furthermore, the potential effects of class imbalance or dataset heterogeneity on the model's accuracy should be analyzed. The criteria for selecting these species and their relevance to the broader scope of stress response studies should be further clarified.
5. Page 9, Lines 70-77: The interaction mechanism between H2O2 and POMs is briefly mentioned. However, a more detailed explanation of how H2O2 oxidizes Mo5+ to Mo6+ and how this leads to changes in NIR absorbance would provide greater clarity. Additionally, the role of oxygen vacancies in enhancing the selectivity toward H2O2 should be further elaborated.

6. Page 9, Lines 79-85: Its advantages over other NIR-II fluorophores in terms of fluorescence efficiency and stability should be quantitatively compared. For example, how does its photostability or quantum yield compare to previously reported NIR-II fluorophores?
7. Page 10, Lines 102-110: The characterization results (e.g., TEM, XPS, zeta potential) provide evidence of successful synthesis. However, it would be helpful to compare the dispersion quality and stability of the nanosensors with and without Mo/Cu-POM assembly. Does the presence of Mo/Cu-POM influence the physical stability or aggregation behavior of the nanoparticles?
8. Page 12, Lines 127-140: It would be helpful to quantify this relationship. For instance, It is suggested to provide data or metrics that compare the degree of spectral overlap to the resulting quenching efficiency for each AIE luminophore.
9. Page 14, Lines 179-184: The lack of significant changes in FV/FM and the propidium iodide assay results strongly support the nanosensor's biocompatibility. It is suggested to briefly discuss whether these observations hold across different environmental conditions (e.g., drought stress or varying light intensities).
10. Page 15, Lines 187-197: Particularly in terms of detection limits and dynamic range, how does the designed nanosensor's sensitivity compare to other reported H_2O_2 sensors.
11. Consider that expanding on the practical implications of achieving a classification accuracy of 96.67%. It could provide a more balanced view by including comments, for example, how might this accuracy translate to real-world applications in agriculture or environmental monitoring? discussing any challenges or limitations encountered during ML implementation.